

SOUTHTRAC-GW

An Airborne Field Campaign to Explore Gravity Wave Dynamics at the World's Strongest Hotspot

Markus Rapp, Bernd Kaifler, Andreas Dörnbrack, Sonja Gisinger, Tyler Mixa, Robert Reichert, Natalie Kaifler, Stefanie Knobloch, Ramona Eckert, Norman Wildmann, Andreas Giez, Lukas Krasauskas, Peter Preusse, Markus Geldenhuys, Martin Riese, Wolfgang Woiwode, Felix Friedl-Vallon, Björn-Martin Sinnhuber, Alejandro de la Torre, Peter Alexander, Jose Luis Hormaechea, Diego Janches, Markus Garhammer, Jorge L. Chau, J. Federico Conte, Peter Hoor, and Andreas Engel



ABSTRACT: The southern part of South America and the Antarctic peninsula are known as the world's strongest hotspot region of stratospheric gravity wave (GW) activity. Large tropospheric winds are deflected by the Andes and the Antarctic Peninsula and excite GWs that might propagate into the upper mesosphere. Satellite observations show large stratospheric GW activity above the mountains, the Drake Passage, and in a belt centered along 60°S. This scientifically highly interesting region for studying GW dynamics was the focus of the Southern Hemisphere Transport, Dynamics, and Chemistry–Gravity Waves (SOUTHTRAC-GW) mission. The German High Altitude and Long Range Research Aircraft (HALO) was deployed to Rio Grande at the southern tip of Argentina in September 2019. Seven dedicated research flights with a typical length of 7,000 km were conducted to collect GW observations with the novel Airborne Lidar for Middle Atmosphere research (ALIMA) instrument and the Gimballed Limb Observer for Radiance Imaging of the Atmosphere (GLORIA) limb sounder. While ALIMA measures temperatures in the altitude range from 20 to 90 km, GLORIA observations allow characterization of temperatures and trace gas mixing ratios from 5 to 15 km. Wave perturbations are derived by subtracting suitable mean profiles. This paper summarizes the motivations and objectives of the SOUTHTRAC-GW mission. The evolution of the atmospheric conditions is documented including the effect of the extraordinary Southern Hemisphere sudden stratospheric warming (SSW) that occurred in early September 2019. Moreover, outstanding initial results of the GW observation and plans for future work are presented.

KEYWORDS: Dynamics; Gravity waves; Mountain waves; Stratospheric circulation; Aircraft observations

<https://doi.org/10.1175/BAMS-D-20-0034.1>

Corresponding author: Markus Rapp, markus.rapp@dlr.de

In final form 23 November 2020

©2021 American Meteorological Society

For information regarding reuse of this content and general copyright information, consult the [AMS Copyright Policy](#).



This article is licensed under a [Creative Commons Attribution 4.0 license](#).

AFFILIATIONS: Rapp—Institut für Physik der Atmosphäre, Deutsches Zentrum für Luft- und Raumfahrt, Oberpfaffenhofen, and Meteorologisches Institut München, Ludwig-Maximilians-Universität München, Munich, Germany; Kaifler, Dörnbrack, Gisinger, Mixa, Reichert, Kaifler, Knobloch, Eckert, and Wildmann—Institut für Physik der Atmosphäre, Deutsches Zentrum für Luft- und Raumfahrt, Oberpfaffenhofen, Germany; Giez—Einrichtung Flugexperimente, Deutsches Zentrum für Luft- und Raumfahrt, Oberpfaffenhofen, Germany; Krasauskas, Preusse, Geldenhuys, and Riese—Institute of Energy and Climate Research (IEK-7), Forschungszentrum Jülich, Jülich, Germany; Woiwode, Friedl-Vallon, and Sinnhuber—Institute of Meteorology and Climate Research, Karlsruhe Institute of Technology, Karlsruhe, Germany; de la Torre—Facultad de Ingeniería, Universidad Austral, LIDTUA (CIC), and CONICET, Pilar, Argentina; Alexander—IFIBA, CONICET, Buenos Aires, Argentina; Hormaechea—Estación Astrónomas Río Grande, Facultad de Ciencias Astronómicas y Geofísicas, Universidad Nacional de La Plata, and CONICET, La Plata, Argentina; Janches—NASA Goddard Space Flight Center, Greenbelt, Maryland; Garhammer—Meteorologisches Institut München, Ludwig-Maximilians-Universität München, Munich, Germany; Chau and Conte—Leibniz Institute of Atmospheric Physics, Kühlungsborn, Germany; Hoor—Institute of Atmospheric Physics, Johannes Gutenberg University of Mainz, Mainz, Germany; Engel—Institute for Atmospheric and Environmental Sciences, Goethe University Frankfurt, Frankfurt, Germany

The region of the southern Andes and the Antarctic Peninsula is known as the world’s strongest stratospheric hotspot of gravity wave (GW) activity (in terms of strength and occurrence frequency) occurring during austral winter and lasting to early spring (e.g., Hoffmann et al. 2013; P. Alexander et al. 2010; de la Torre et al. 2012; Llamedo et al. 2019). Known sources of GWs are flow over orography [in which case the GWs are called mountain waves (MWs)], convection, and spontaneous emission (Fritts and Alexander 2003; Plougonven and Zhang 2014). While intense MW activity is expected above and in the lee of the mountains given the prevailing strong tropospheric westerly winds, it is, however, somewhat surprising that strong GW activity is observed in the middle to upper stratosphere along 60°S spinning from the Drake Passage to the South Pacific (see, e.g., Ern et al. 2006; M. J. Alexander et al. 2010; Hindley et al. 2015; and Fig. 1 for illustration). This circumpolar

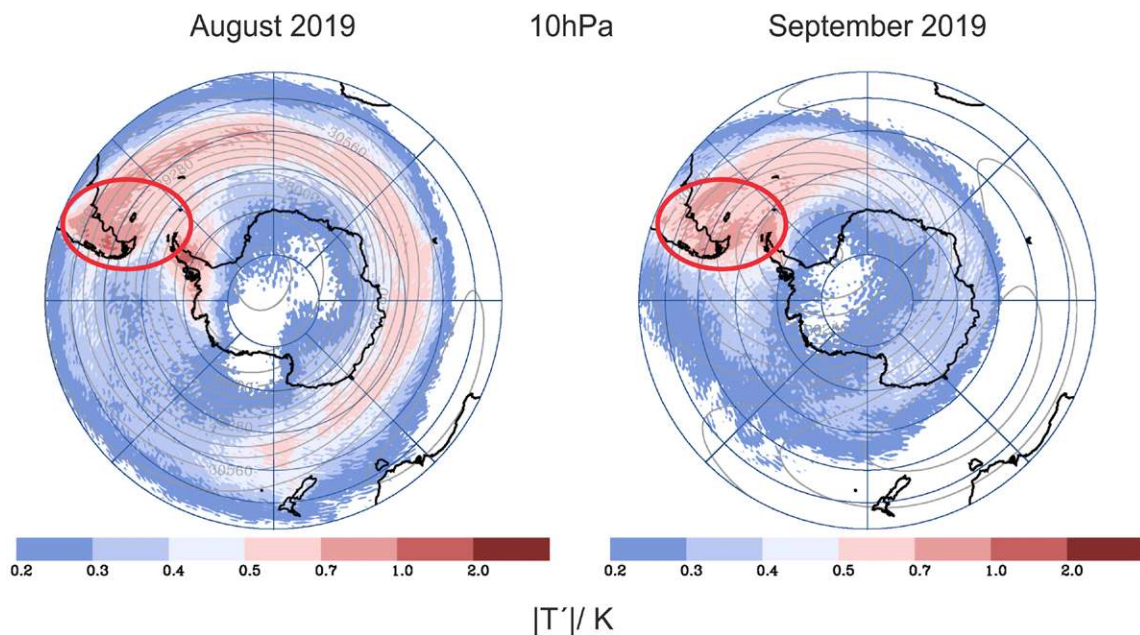


Fig. 1. Illustration of the GW belt based on ERA5 temperature perturbations for (left) August and (right) September 2019 at a pressure levels of 10 hPa. Shown is $|T'| = \sqrt{(T_{639} - T_{106})^2}$ (K; see “Models” section for details). The red oval marks the target area where airborne measurements were conducted during SOUTHTRAC-GW.

band of almost zonally symmetric GW activity and related momentum fluxes will be referred to as the “gravity wave belt.”

While observational evidence for the GW belt is undisputed, state of the art climate models fail to reproduce this feature with important consequences (McLandress et al. 2012; Geller et al. 2013). The “missing drag at 60°S” in the models leads to a too strong polar night jet (PNJ) and hence to too low temperatures in the southern polar winter stratosphere known as the “cold pole bias” of climate models affecting the polar stratospheric cloud formation and heterogeneous ozone chemistry [Butchart et al. 2011; Stratosphere–Troposphere Processes and Their Role in Climate (SPARC); SPARC 2010]. In addition, the breakdown of the polar vortex is simulated to occur too late in spring leading to a lagged recovery of the Antarctic ozone hole (Austin et al. 2003; McLandress and Shepherd 2009). McLandress et al. (2012) showed that adding artificial MW drag along 60°S in a numerical experiment resulted in more realistic stratospheric winds and higher polar temperatures. In the same spirit, Garcia et al. (2017) enhanced the orographic GW (OGW) forcing in the SH by simply doubling the magnitude of sources to achieve more realistic climatologies of tropospheric and stratospheric winds, temperatures, and ozone concentrations. However, they also showed that a parameterization for non-OGWs (NOGW) leads to similar improvements of wind and temperature climatologies. Thus, OGWs play an important role, but also NOGW sources likely contribute to the “missing drag at 60°S” (see also Cámara et al. 2016; Holt et al. 2017).

Accordingly, several different physical processes, involving both OGW and NOGW, have been proposed to account for the observed belt of enhanced stratospheric GW momentum fluxes around 60°S: These are 1) downwind advection and meridional refraction of OGW from the southern Andes and the Antarctic Peninsula into the PNJ (Dunkerton 1984; Preusse et al. 2002; Sato et al. 2009, 2012); 2) unresolved OGWs from small islands (Alexander and Grimsdell 2013; Alexander et al. 2009; Vosper 2015; Pautet et al. 2016; Eckermann et al. 2016); 3) the generation of secondary waves in the breaking regions of these primary orographic waves (Satomura and Sato 1999; Hindley et al. 2015); 4) NOGWs from sources associated with winter storm tracks over the Southern Ocean (Wu and Eckermann 2008; Hendricks et al. 2014; Plougonven et al. 2015) or with convection and frontogenesis (Choi and Chun 2013; Holt et al. 2017); 5) and finally, a zonally uniform distribution of small amplitude waves from nonorographic mechanisms such as spontaneous adjustment and jet instability around the edge of the stratospheric PNJ (Sato and Yoshiki 2008; Hindley et al. 2015, 2019).

It is hence obvious that the Southern Hemisphere region around 60°S is a scientifically highly interesting target for studying GW processes and their impact on the stratospheric circulation and climate. Already in the austral winter of 2014 the Deep Propagating Gravity Wave Experiment (DEEPWAVE) conducted research flights with two aircraft from Christchurch, New Zealand, and involved various ground based instruments, satellite datasets, as well as a variety of numerical models of different complexity (Fritts et al. 2016). DEEPWAVE was also the first comprehensive airborne mission studying GW dynamics up to the mesopause (~100 km). To mention just a few outstanding results, DEEPWAVE provided insight into the relation between tropospheric forcing and GW activity in the middle atmosphere (Fritts et al. 2016, 2018; Kaifler et al. 2015; Bramberger et al. 2017; Portele et al. 2018), the horizontal propagation of OGW into the polar night jet (Ehard et al. 2017), secondary wave generation in regions of strong MW breaking (Bossert et al. 2017), the effect of the background atmosphere on GW propagation also in the absence of critical level filtering (Kruse et al. 2016), the relative contribution of various parts of the GW spectrum to momentum fluxes (Smith et al. 2016; Smith and Kruse 2017, 2018; Bossert et al. 2018), and the general characteristics of both OGWs and NOGWs (Smith et al. 2016; Smith and Kruse 2017; Eckermann et al. 2016; Pautet et al. 2016, 2019; Jiang et al. 2019).

DEEPWAVE explored mainly GWs over the Southern Alps at about 45°S and only few flights went down to latitudes south of 55°S (Fig. 2 of Pautet et al. 2019). As a complementary experiment to DEEPWAVE and targeting the Southern Hemisphere GW hotspot, the Southern Hemisphere Transport, Dynamics, and Chemistry–Gravity Waves (SOUTHTRAC-GW) airborne research mission with the German High Altitude and Long Range Research Aircraft (HALO) was conducted from Rio Grande, Tierra del Fuego, Argentina (53°S, 67°W), as part of the more comprehensive SOUTHTRAC mission (see www.pa.op.dlr.de/southtrac/science/scientific-objectives/). The objectives of SOUTHTRAC-GW are summarized in Table 1.

In the second section, we describe the research aircraft and its instruments dedicated to the measurements of GW properties, along with the ground based measurements in the region. We will introduce the forecast model tools used for flight planning as well as re-analysis fields which are being used for the interpretation of atmospheric measurements. In the third section, we describe the prevailing meteorological conditions under which the flights were conducted. Mission overview and initial promising results are presented in the fourth section. The article closes with a summary and outlook on ongoing and planned analysis work in the fifth section.

Instruments and datasets

HALO and airborne instruments. The German research aircraft HALO is based on a Gulfstream G550 business jet with a maximum range of ~8,000 km, a maximum flight altitude of ~15 km, and a typical cruise speed of ~800 km h⁻¹ (cf. Fig. 2, upper- and lower-left panels). It has been modified to allow gas sampling and optical experiments in the cabin and to mount several

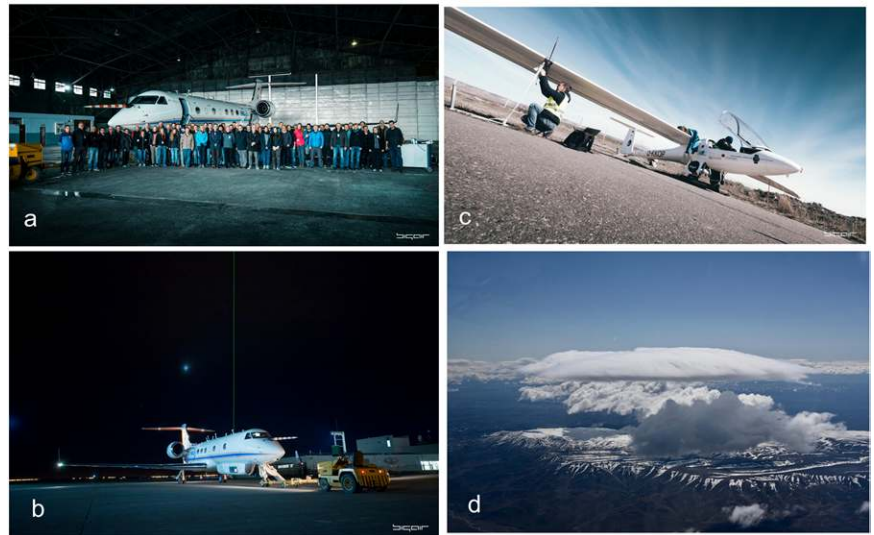


Fig. 2. (a) Group photo of the campaign participants of the SOUTHTRAC-GW mission in front of the HALO aircraft inside the hangar of the naval air base in Rio Grande. (b) HALO aircraft outside the hangar of the naval air base in Rio Grande during a test run of the ALIMA instrument with its green laser beam pointing upward. (c) DLR scientist Norman Wildmann mounting a 5-hole probe to measure meteorological parameters on the Stemme aircraft of glider pilot Klaus Ohlmann. (d) Impressive MW cloud over the southern Andes as seen during a flight of the Stemme.

Table 1. Scientific objectives of SOUTHTRAC-GW.

No.	Objective
1	Yield coordinated observations in the troposphere, stratosphere, and mesosphere for the early propagation of OGWs excited over the southern Andes and/or Antarctic Peninsula into the PNJ
2	Better quantify the mountain waves in the vicinity of their sources and document the early stages of their vertical and horizontal propagation
3	Provide unprecedentedly detailed measurements for comparison and validation of high-resolution simulations that can resolve, in case studies, much of the GW spectrum
4	Explore the breaking and dissipation of the GWs, including the excitation of secondary GW
5	Compare the identification of GW as seen by different measurement techniques

spectrometers under the wings as well as a “belly pod” under its fuselage to carry large instruments (Krautstrunk and Giez 2012). In total, HALO may carry up to three tons of scientific payload. HALO has been in service since 2012 and has by now been used in scientific missions addressing a broad spectrum of atmospheric chemistry and physics research objectives (e.g., Wendisch et al. 2016; Voigt et al. 2017; Schäfler et al. 2018; Stevens et al. 2019; Oelhaf et al. 2020).

During SOUTHTRAC-GW there were three prime instruments dedicated to the measurements of GW signatures, namely, the novel Airborne Lidar for Middle Atmosphere research (ALIMA), the Gimballed Limb Observer for Radiance Imaging of the Atmosphere (GLORIA), and the Basic HALO Measurement and Sensor System (BAHAMAS).

As deployed during SOUTHTRAC-GW, ALIMA is a compact upward pointing Rayleigh lidar using a pulsed neodymium-doped yttrium aluminum garnet (Nd:YAG) laser transmitting 12.5 W (125 mJ) at 532 nm with a 48-cm diameter receiving telescope, and using three height-cascaded elastic detector channels to yield atmospheric density profiles in the altitude range from 20 to 90 km. Density profiles are converted to temperatures using hydrostatic downward integration (Hauchecorne and Chanin 1980). For typical horizontal and vertical integration intervals of 10 and 1 km, respectively, temperatures are derived between 20- and 80-km altitude. From 20 to 60 km the corresponding error is 0.9 K, from 60 to 70 km it is 2.9 K, and above it is 6.5 K. From 20 to 60 km the error is near constant because the signal is distributed over the three height-cascaded detector channels. To separate GW-induced temperature perturbations from atmospheric background temperatures a 30-min running mean (corresponding to a flight distance of ~400 km) is applied.

The infrared limb imager GLORIA performs two-dimensional and tomographic measurements of temperatures and trace gas mixing ratios (Friedl-Vallon et al. 2014; Riese et al. 2014). For this purpose, GLORIA combines a Michelson interferometer with a 2D infrared detector and measures molecular thermal emissions in the spectral range between 780 and 1,400 cm^{-1} (7.1–12.8 μm). GLORIA is mounted in the belly pod. Its line of sight aims toward the horizon on the right side of the aircraft and measures infrared radiation emitted by molecules in the atmosphere. The horizontal observation angle is varied from 45° to 135° with respect to the flight direction. In this way, the instrument can investigate the same air volume from different directions, which allows for a tomographic retrieval scheme (Ungermann et al. 2011; Kaufmann et al. 2015; Krisch et al. 2018). In the vertical, GLORIA may sample the atmosphere from ~1 km above cruise altitude down to approximately 5-km altitude (below which the investigated spectral lines become optically thick). GLORIA was applied under different measurement strategies to the observation of GW (Krisch et al. 2017, 2020). GW effects on the distribution of trace gases were investigated by Woiwode et al. (2018) and Kunkel et al. (2019).

While GLORIA and ALIMA enable characterization of the atmosphere below and above the aircraft, respectively, the BAHAMAS system consists of a nose tip probe with a 5-hole wind sensor and yields in situ measurements of horizontal and vertical winds along with temperatures and pressures at flight level at high temporal resolution, i.e., of up to 100 Hz (Giez et al. 2017, 2019). Corresponding data have been successfully used for the derivation of momentum and energy fluxes owing to GW as well as for turbulence analysis (Bramberger et al. 2017; Portele et al. 2018; Bramberger et al. 2020; Gisinger et al. 2020; Wilms et al. 2020).

Finally, besides HALO a Stemme S10VT motor glider (cf. Fig. 2, upper-right panel) was also deployed to the nearby city of El Calafate (cf. Fig. 8) and equipped with another 5-hole probe to measure temperature and wind distributions in the MWs over the southern Andes (see Fig. 2, lower-right panel, for a photo taken from the cockpit of the Stemme during one of the glider flights).

Ground-based and satellite instruments and radiosondes. The Estación Astrónomicas Río Grande (EARG), which is located close to the airport of Rio Grande, hosts a number of ground based instruments that were useful as supplementary observations to the airborne measurements. For SOUTHTRAC-GW the Compact Rayleigh Autonomous Lidar (CORAL) (Kaifler and Kaifler 2020; Reichert et al. 2019) and the Southern Argentina Agile Meteor Radar (SAAMER) (Fritts et al. 2010b) provided important background information on middle atmosphere temperature, winds, and momentum fluxes, respectively.

CORAL measures atmospheric density from roughly 15–90-km altitude. The Rayleigh lidar emits 12-W power at 532-nm wavelength and receives backscattered photons with a 63-cm diameter telescope using three height-cascaded elastic detector channels and one Raman channel. As in the case of ALIMA, density profiles measured with CORAL are converted to temperature profiles using hydrostatic downward integration. CORAL is a portable lidar and commenced operation at EARG in November 2017. CORAL operates autonomously during clear sky conditions in darkness. Weather conditions are continuously and automatically assessed based on local observations and short-term weather forecasts of clouds and precipitation. CORAL lidar data were used to study a long-term, large-amplitude stratospheric mountain wave event, and was combined with another lidar and satellite data to spatially resolve the structure of a GW (Kaifler et al. 2020; Alexander et al. 2020).

SAAMER is a meteor radar which detects specular reflections of radio waves transmitted at 32.55 MHz from meteor trails. The peak transmitted power of 4 kW is distributed over eight simultaneous beams at 35° off zenith and 45° azimuth increments. For each meteor detection, the radial velocity of the advected meteor trail is determined. By fitting all radial velocities that are measured during a time interval of one hour, the mean horizontal wind vector over that period and the altitude range between 80 and 100 km—where most meteors are detected—is determined. Furthermore, momentum fluxes are estimated from the observations by application of a generalization of the dual-beam technique of Vincent and Reid (1983) using the formulation derived by Hocking (2005). Studies of mean wind, tides, and momentum fluxes have been published for example by Fritts et al. (2010b,a), and de Wit et al. (2017), respectively. In addition, SAAMER is also used for astronomical studies of sporadic meteors as well as meteor showers (Janches et al. 2015, 2020; Bruzzone et al. 2020). Since May 2019, SAAMER has been augmented with two additional receiving stations at Tolhuin and Ushuaia [Multistatic, Multifrequency Agile Radar for Investigations of the Atmosphere (MMARIA)-SAAMER] to perform multistatic measurements. The multistatic configuration allows more meteor detections, different viewing angles, and the estimation of the horizontal wind fields inside the illuminated volume (Stober and Chau 2015; Chau et al. 2017). For example, vertical winds free from horizontal divergence contamination are obtained using a gradient method (Chau et al. 2020).

To complement the CORAL lidar measurements, radio occultation (RO) measurements from the operational MetOp satellites as well as Sounding of the Atmosphere Using Broadband Emission Radiometry (SABER) limb sounding measurements complement the CORAL lidar measurements. The RO technique yields profiles of temperature and GW potential energy density (GWPED) between 20- and 40-km altitude. Temperature perturbations needed to determine GWPEDs were determined from RO temperature profiles by applying a fifth-order Butterworth filter with a vertical cutoff wavelength of 15 km. Characteristics and quality of this dataset are described in Rapp et al. (2018a) and the data have recently been used in a study of midlatitude inertial instability in Rapp et al. (2018b). SABER limb sounding measurements also yield temperature profiles from 20- up to ~100-km altitude (Remsberg et al. 2008) and are used at times when no CORAL or ALIMA measurements are available (i.e., from the beginning of August to the beginning of September) to characterize

the mesospheric temperature background. In addition, GW momentum fluxes will be deduced following Ern et al. (2018).

Finally, a total of 59 radiosondes were released at Rio Grande (29 sondes) and El Calafate (30 sondes) during the September deployment of the HALO aircraft. At Rio Grande, a GRAW sounding system with DFM-09 radiosondes (pressure determined by GPS) was used (GRAW 2019), whereas at El Calafate a Vaisala sounding system with RS41 (some sondes with pressure sensor) was employed (Vaisala 2020). The sondes yielded profiles of temperature, pressure, humidity, and wind up to typical maximum altitudes of 25–30 km at a vertical resolution of 5–10 m depending on ascent rate. Table 2 summarizes all measurements available for the characterization of GWs during SOUTHTRAC-GW.

Models. Flight planning for the HALO research flights was conducted with a lead time of five to two days using the operational, deterministic forecasts of the Integrated Forecasting System (IFS) of the European Centre for Medium-Range Weather Forecasts (ECMWF) and the Met Office Unified Model. For the interpretation of the observational dataset we further use ERA5 data. ERA5 is a global reanalysis dataset that is based on the IFS in cycle CY41R2 with 137 hybrid sigma/pressure (model) levels in the vertical, with the top level at 0.01 hPa.

This IFS cycle uses a sponge layer that starts at 10 hPa damping vertically propagating GWs (Polichtchouk et al. 2017). Ehard et al. (2018) compared ground based lidar measurements of GWs with corresponding IFS results and found that wave amplitudes are indeed underestimated in the sponge layer. In addition, the sponge damps the zonal mean flow though the small wavenumbers do not experience a very strong damping by the hyperdiffusion type of damping (Polichtchouk et al. 2017). With respect to mesospheric temperatures, the damping of GWs in the sponge layer weakens the upwelling (i.e., cooling) in the summer hemisphere and the downwelling (i.e., warming) in the winter hemisphere (Polichtchouk et al. 2017).

So far, ERA5 covers the period from 1979 to present. The high-resolution output is available every hour and has a horizontal resolution of 31 km. For more details see Hersbach et al. (2020). In some instances, we will show GW-induced temperature perturbations that are obtained as $T' = T_{639} - T_{106}$; i.e., we subtract ERA5 temperatures at the same spatial resolution but spectrally reduced to T106 from the full-resolution T639 fields.

Table 2. Airborne, ground-based, and satellite measurements suitable for characterization of GW during SOUTHTRAC-GW. The variables u , v , w , n , p , RH, T denote zonal, meridional, and vertical wind, number density, pressure, relative humidity, and temperature. The terms du/dx and dv/dx denote horizontal gradients of u and v ; Δz is vertical and Δx and Δy horizontal resolution (in two dimensions).

Instrument	Platform	Measured quantity	Height range	Resolution	Reference
ALIMA	HALO	n, T	20–90 km	$\Delta z = 1$ km, 50 s	This study
GLORIA	HALO	T , trace gases	5–15 km	$\Delta z = 200$ m, $\Delta x = 20$ km $\Delta y = 20$ km	Riese et al. (2014), Friedl-Vallon et al. (2014)
BAHAMAS	HALO	u, v, w, T, p	In situ, 15 km	100 Hz	Giez et al. (2017)
CORAL	Rio Grande	n, T	15–95 km	1 km, 1 h	Kaifler and Kaifler (2020)
SAAMER	Rio Grande	$u, v, \overline{u'w'}, \overline{v'w'}$	80–100 km	3 km, hourly	Fritts et al. (2010a)
MMARIA-SAAMER	Multistatic	$u, v, w, du/dx, dv/dx$	80–100 km	2 km, hourly	Chau et al. (2017)
5-hole probe	Stemme	u, v, w, T, p	In situ 0–9 km	10 Hz	Wildmann et al. (2021)
SABER	Satellite	Temperature	0–100 km	$\Delta z = 2$ km, 3° along orbit	Remsberg et al. (2008)
<i>MetOp-A</i> and <i>MetOp-B</i>	Operational satellite	T	20–40 km	$\Delta z = 1$ km	Rapp et al. (2018a)
Radiosondes	Rio Grande	u, v, T, p, RH	0–30 km	$\Delta z = 5$ –10 m	GRAW (2019)
Radiosondes	El Calafate	u, v, T, p, RH	0–30 km	$\Delta z = 5$ –10 m	Vaisala (2020)

Flight planning of the glider flights in El Calafate was supported by the National Met Service of Argentina (Servicio Meteorológico Nacional) who provided dedicated forecasts with the Weather Research and Forecasting (WRF) Model.

Atmospheric conditions during the campaign period

The austral winter and spring season 2019 was unique in the sense that the southern polar vortex in late austral winter 2019 broke down early due to an SSW (Lin et al. 2020). According to classic metrics, it was a minor SSW, but it appeared as a major event as it changed the propagation conditions for MW markedly in September 2019. Already in August 2019, the vortex was offset slightly from the pole compared to the previous years and its shape became more elongated. The disturbance became striking in September 2019 when the vortex area shrunk and the center was displaced toward South America (cf. Fig. 8 in Dörnbrack et al. 2020).

The remarkable weakening and warming of the polar vortex in the period from August to September is illustrated by the comparison of the zonal mean zonal wind and temperature in 2019 with the 41 years long ERA5 climatology in Fig. 3. As depicted in Fig. 3, the zonal mean winds of the PNJ did not only decrease drastically but also its core was shifted poleward and downward compared to the climatology. Another striking feature is the strong negative wind anomaly near the equator at around 10 and 1 hPa extending to 15°–20°S. This anomaly is related to the easterly phase of the quasi-biennial oscillation (QBO; see also the MERRA-2 analyses shown at https://acd-ext.gsfc.nasa.gov/Data_services/met/qbo). The magnitude of the warming amounts to about 30 K (see lower-right panel in Fig. 3 at latitudes south of 80°S).

Associated with the warming in 2019, the zonal winds at ~1 hPa reversed suddenly at the beginning of September and remained negative or close to zero for the rest of the year. This

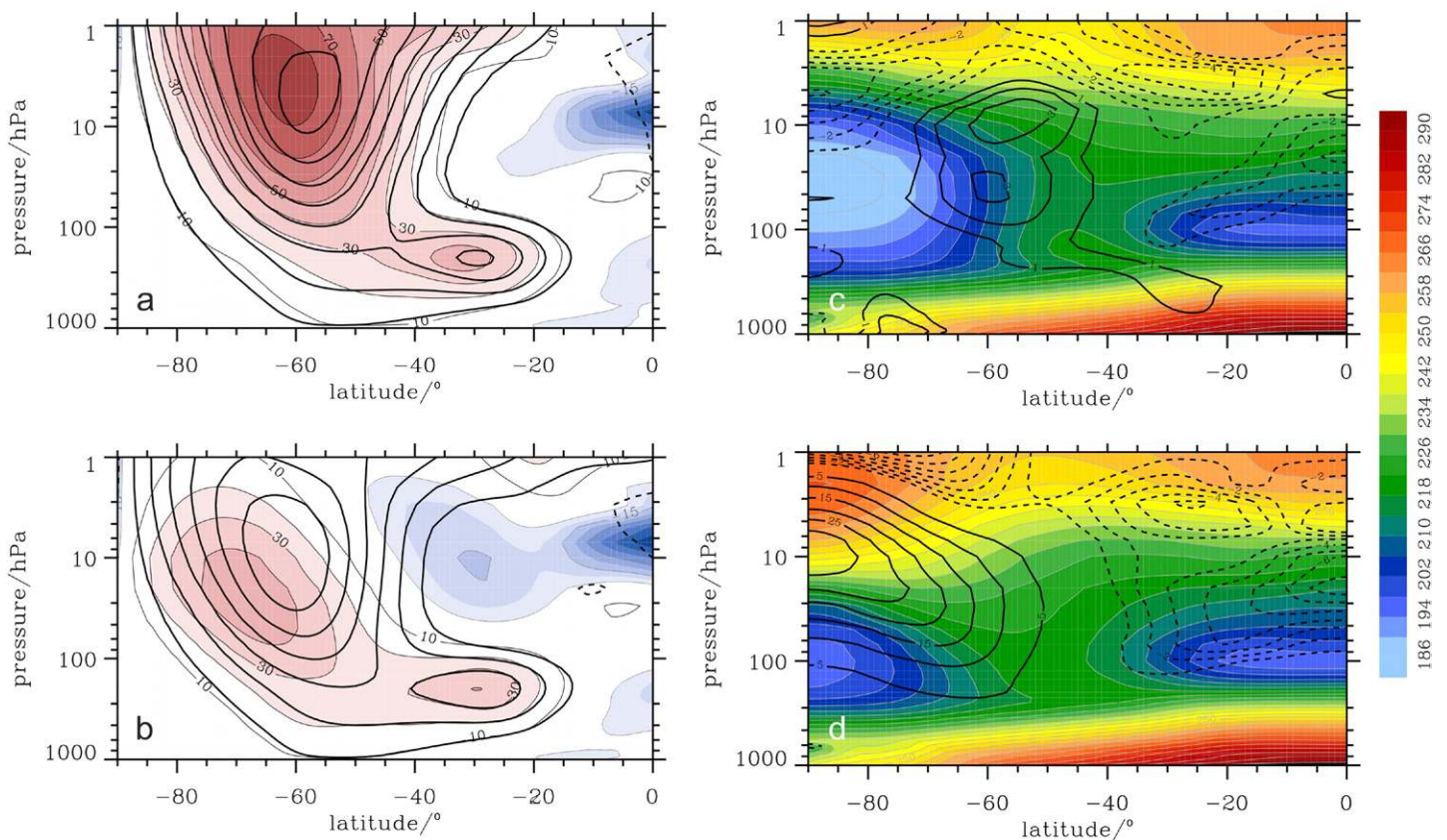


Fig. 3. (left) Zonal mean zonal winds (m s^{-1}) for (a) August and (b) September 2019. Color shading is ERA5 data for the year 2019. Thick black lines are zonal mean winds (10 m s^{-1} increments) from the ERA5 climatological mean from 1979 to 2019. The dashed black line is $u = 0$. (right) Color shading is ERA5 zonal mean temperature (K) for (c) August and (d) September 2019. Thick black lines are temperature anomalies (5-K increments) from the ERA5 climatological mean from 1979 to 2019.

evolution generated a critical level for stationary MWs and confined their vertical propagation to altitudes below about 40 km from 13 September 2019 onward. This effect is clearly illustrated in Fig. 4 depicting the altitude–time sections of the horizontal wind ($V_{HOR} = \sqrt{u^2 + v^2}$, where u and v are zonal and meridional wind) and the wind direction calculated in a box upstream of Patagonia (see also Fig. 8). Frequent weather systems approaching South America produced a sequence of tropospheric jets near 10-km altitude and led to the quasi-continuous low-level forcing of MWs. In the upper stratosphere, the PNJ weakened gradually during the first half of September 2019, the wind reversed from westerlies to easterlies as indicated by

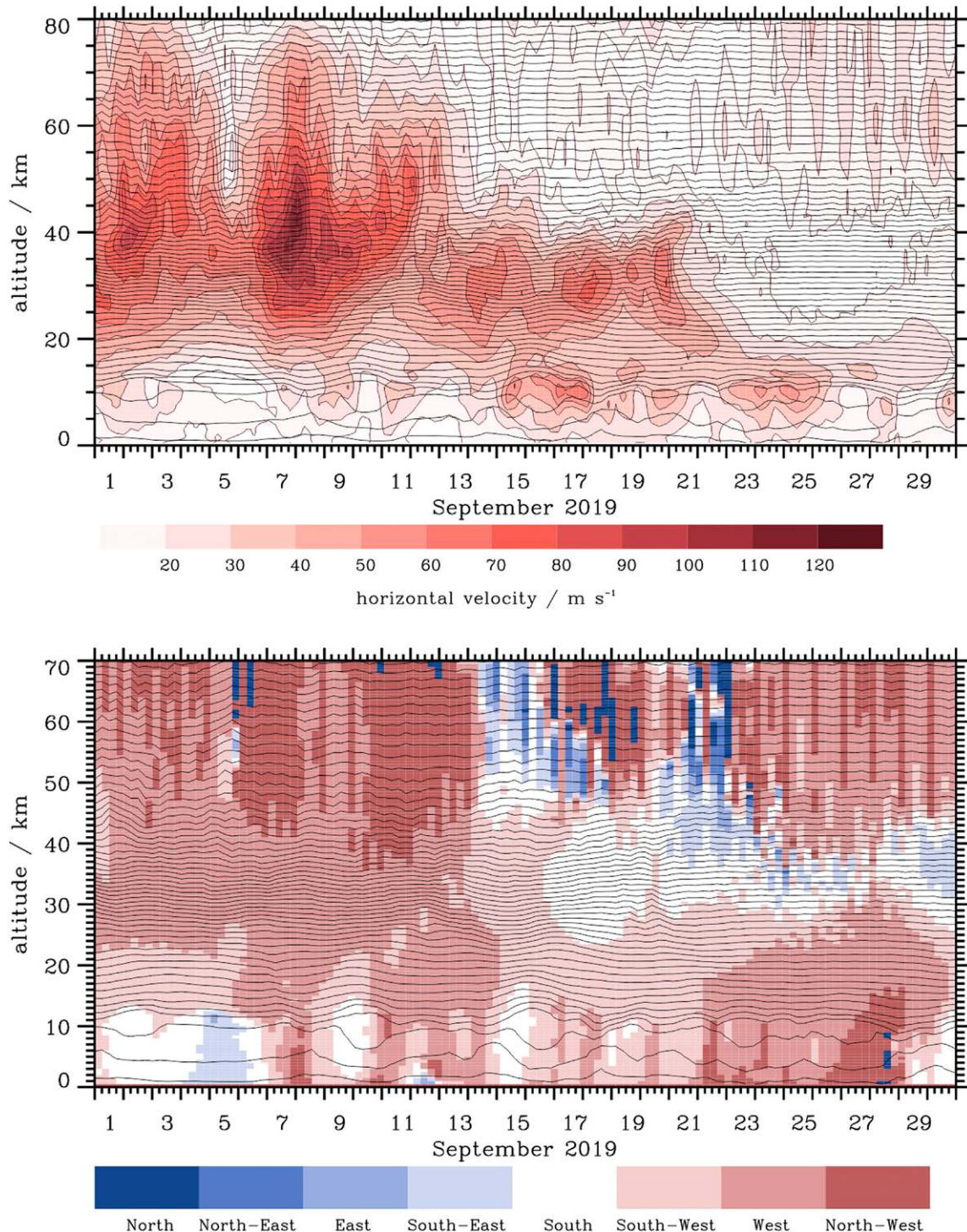


Fig. 4. Upstream profiles of ERA5 (top) horizontal wind V_{HOR} and (bottom) wind direction for September 2019. The data are averaged in the upstream box ($80^{\circ}W \pm 5^{\circ}$, $50^{\circ}S \pm 5^{\circ}$).

the 180° change of the wind direction. At the end of the month only the tropospheric jets and the tides remained as high wind patterns upstream of South America.

To illustrate the spatial transitions of VHOR, of the geopotential height Z , and of the absolute temperature T associated with the stratospheric warming event, we show their respective anomalies $VHOR^*$, Z^* , and T^* for August and September 2019 related to the 41-yr ERA5 climatological mean at 100 hPa in Fig. 5. The warming and horizontal shift of the cold center of the polar vortex toward South America is clearly visible in the T^* plots. The T^* amplitude increased from August to September to values up to 25 K. Associated with this T anomaly is the Z anomaly that switched from a weak planetary wave-2 (PW2) pattern in August to a strong PW1 pattern in September (see also Shen et al. 2020). In September, related to the weakening and shrinking of the polar vortex, VHOR over Patagonia decreased south of 50°S and increased north of about 50°S leading to weaker than normal winds toward Antarctica.

Notably, the effect of the SSW can also be clearly seen in middle atmosphere temperature and wind measurements acquired at EARG as well as in MetOp RO measurements in the region (Figs. 6 and 7). Figure 6 shows daily mean (i.e., tidal components removed) zonal wind measurements from SAAMER for the period 1 July–31 December 2019. The mesospheric observations show mainly westerly winds with maximum values of about 50 m s⁻¹ until 12 September after which the winds at all observed altitudes changed to easterly direction with maximum values of about 20 m s⁻¹ until the end of October. Hence, the mesospheric circulation

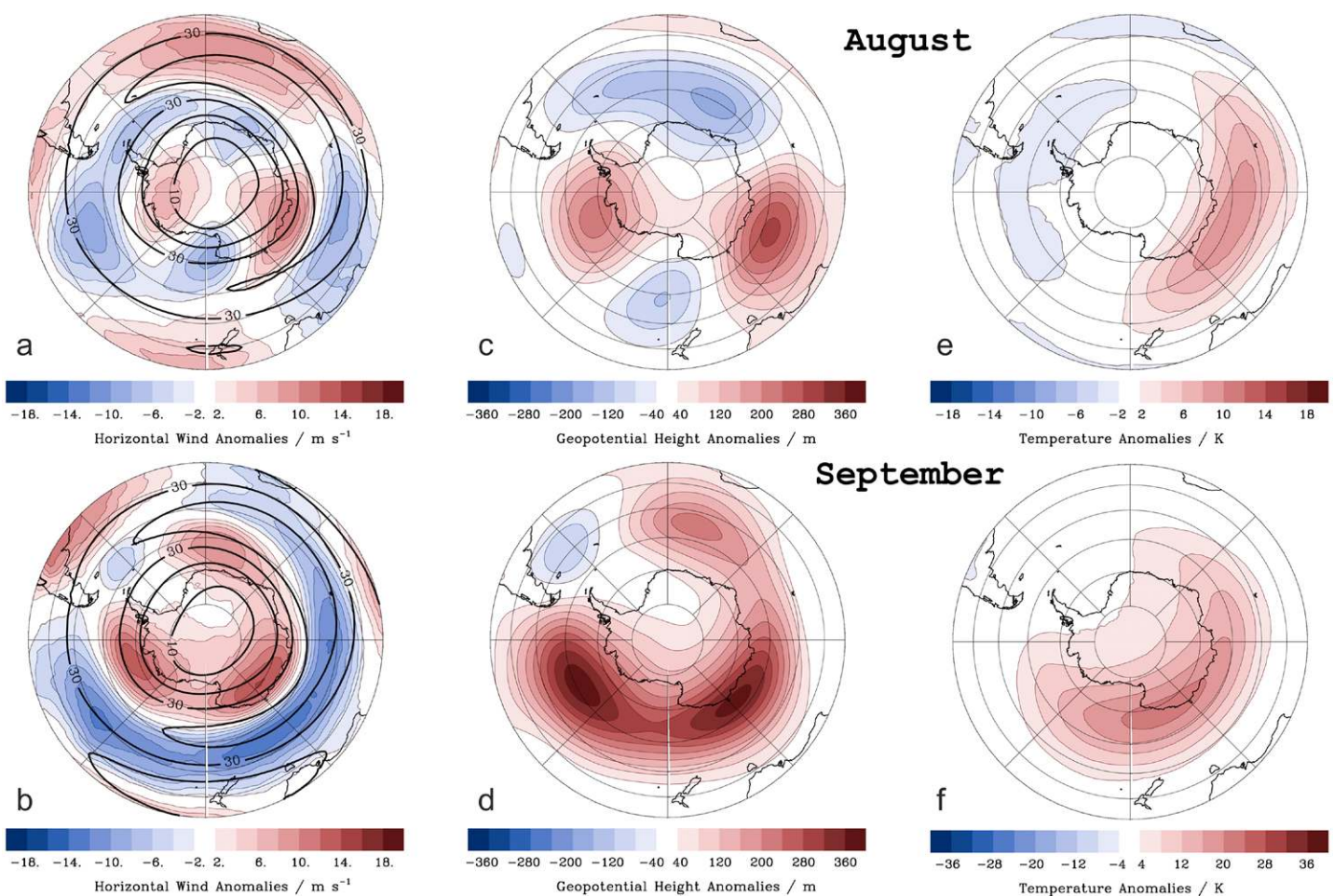


Fig. 5. Color shading shows anomalies of the (a),(b) horizontal wind, (c),(d) geopotential height, and (e),(f) temperature at 100 hPa with respect to the 41-yr ERA5 climatological mean for (top) August and (bottom) September 2019. The black lines in the left column show the mean wind. Note, the temperature scale is different for August and September.

changed to a summer-like state as early as in the middle of September. In the climatological mean the transition would be expected to occur about one month later (de Wit et al. 2017). This early transition to a summer-like state is well known from corresponding mesospheric wind observations in the Northern Hemisphere as being due to the changed GW propagation characteristics during SSW (Hoffmann et al. 2002). Interestingly, the wind structure in the period from 12 September until the end of October also deviates from a typical summer circulation since easterly winds are observed in the entire SAAMER observation volume whereas in the climatological mean easterly winds are only expected below ~90 km, with westerly winds usually occurring above. Hence, the unusual filtering conditions for GW in the stratosphere coincided with a very unusual mesospheric circulation

in the entire altitude range from 80 to 100 km as probed by SAAMER. Only after the beginning of November, a typical summer circulation is observed (cf. to Fig. 3 in de Wit et al. 2017).

The composite of CORAL, SABER and ALIMA temperature measurements in the upper stratosphere and mesosphere also reveals characteristic signatures as expected for an SSW (lower panel of Fig. 6). Already in the end of August, the stratopause moves up, which is in agreement with several previous observations and modeling studies of SSW effects on the mesosphere (e.g., Siskind et al. 2010; Limpasuvan et al. 2016). After the beginning of November, CORAL measured a cold summer mesopause with temperatures falling as low as 150 K above ~80-km altitude, which is consistent with the SAAMER observations of a summer circulation after the same date.

To get a first impression of the temporal evolution of stratospheric GW activity in the region we next turn to the MetOp RO measurements of temperatures and GWPED in Fig. 7. Here, we clearly see signatures of the SSW in both parameters in the stratosphere. The shown RO measurements are daily averages over a box range from 55° to 64°S and from 70° to 0°W, which is the region of the Drake Passage and eastward along the Southern Ocean centered at 60°S. This averaging has been chosen due to the scarce sampling of the MetOp satellites at these latitudes [see Fig. 1a in Rapp et al. (2018b) for typical daily sampling statistics of MetOp RO measurements]. Figure 7 clearly

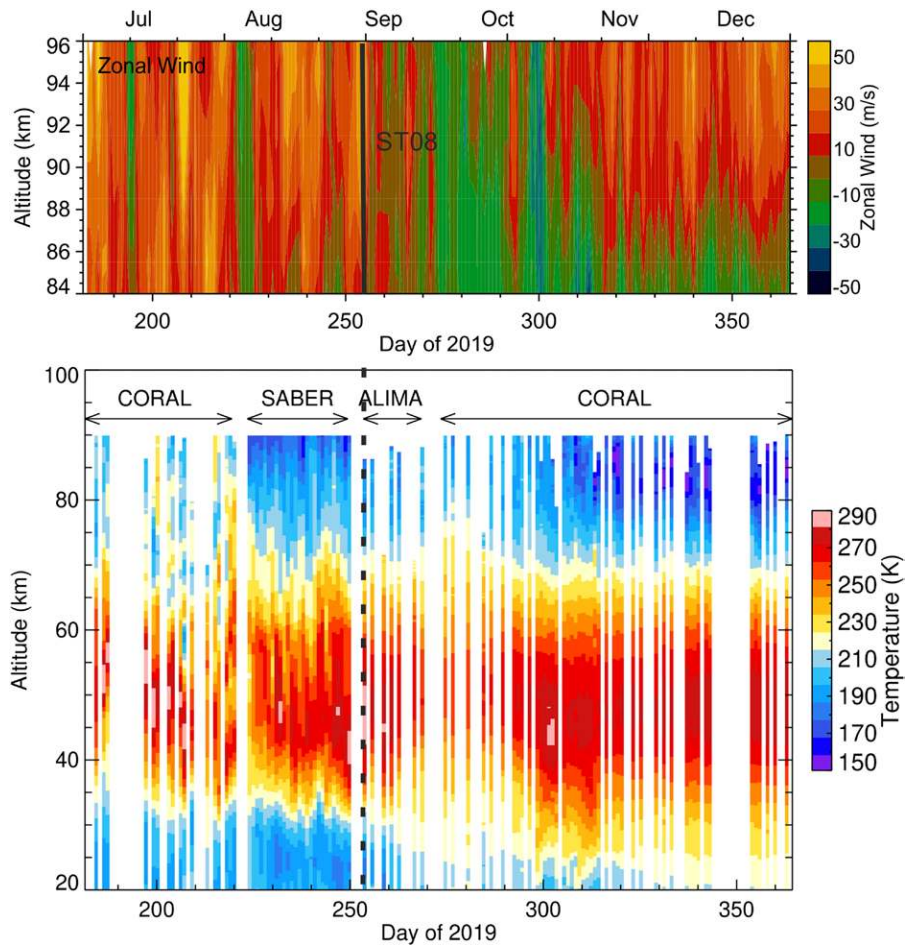


Fig. 6. (top) Zonal wind measurements during July–December 2019 with SAAMER. (bottom) Composite of lidar measurements with the ground based system CORAL and ALIMA. From the beginning of August to the beginning of October the laser of the CORAL system failed such that no ground based measurements are available during this time. The gap is partly filled with SABER data and with data from the ALIMA system from HALO flight legs in the vicinity of Rio Grande. In both panels, the black vertical line marks the time of HALO flight ST08.

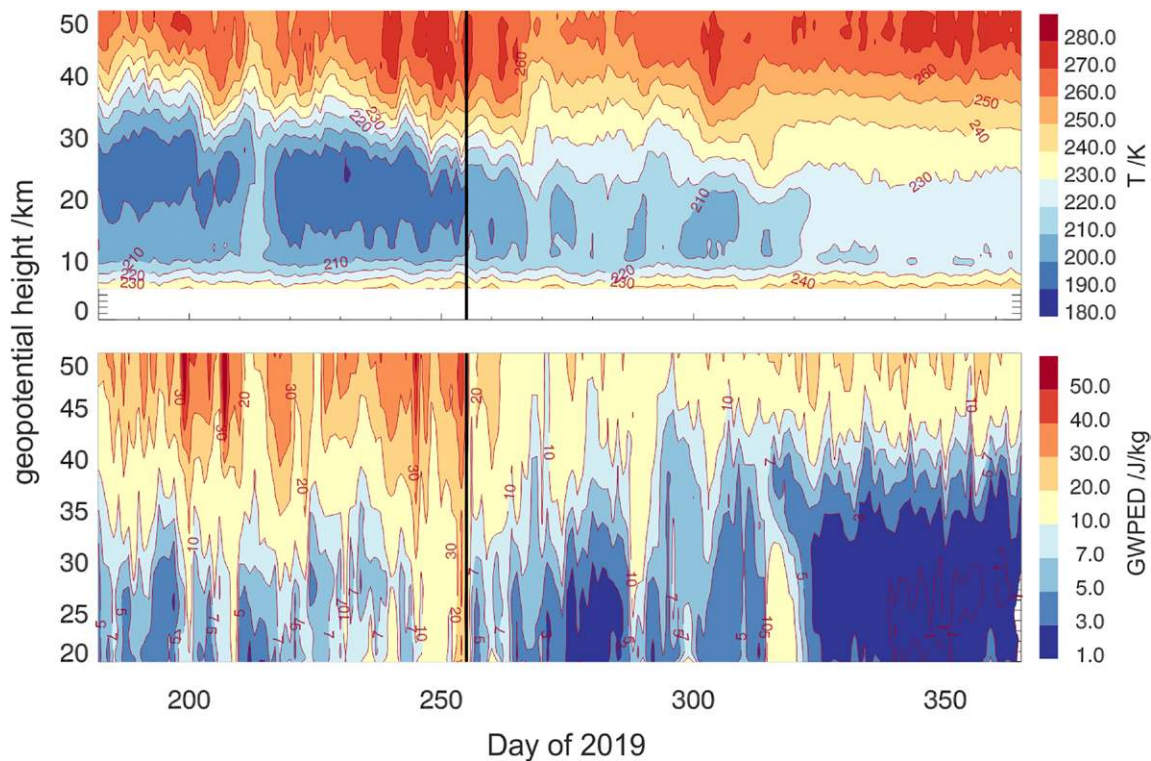


Fig. 7. (top) Stratospheric temperatures (as mean for 55° – 64° S and 70° – 0° W) obtained from radio occultations on board the *MetOp-A* and *MetOp-B* satellites (Rapp et al. 2018a). (bottom) Corresponding GW potential energy densities, also from *MetOp-A* and *MetOp-B*. In both panels, the black vertical line marks the time of HALO flight ST08.

shows a sudden and notable increase of stratospheric temperatures after 12 September (marked with the black vertical line). Even more interesting, right after this date the observed GWPEDs decrease rapidly above ~ 40 km as a consequence of the critical level for MWs seen in Fig. 4.

In summary, the SOUTHTRAC-GW mission took place during the evolution of a rare Southern Hemisphere minor SSW, which had pronounced effects on the propagation characteristics of GW and thus also on the background state of the middle atmosphere.

Mission overview and early results

SOUTHTRAC-GW commenced on 9 September 2020 with the transfer flight from Buenos Aires to Rio Grande followed by six research flights until 26 September. The six local research flights started from and returned to the naval air base at Rio Grande airport and were conducted in darkness to guarantee optimal operation conditions for ALIMA. During all flights, successful measurements with the airborne instruments as listed in Table 2 were obtained. Partly, the ALIMA measurements were deteriorated due to icing on its optical window in the aircraft fuselage. This led to signal degradation and hence a limited altitude coverage during two of the flights (ST07, ST10). Overall, the data quality of ALIMA and all other GW instruments was above expectations to achieve the scientific goals of the mission.

The flight tracks of all seven GW-related research flights are shown in Fig. 8. The general strategy for the planning of these flights was to both observe excitation regions, e.g., over the Andes or over the Antarctic peninsula (see corresponding cross mountain legs), and then to follow the waves into and along the polar vortex. Hence, many flight legs are long and straight at a constant pressure altitude to allow for optimal sampling of GW characteristics. Hexagon-shaped flight tracks were designed for tomographic characterization of tropospheric GW close to their source with GLORIA (i.e., flight tracks of ST12 and ST14). The location of the cross mountain legs as shown in Fig. 8 reflects the fact that during most of the research

flights MW forcing occurred to the north of Rio Grande.

Vertical profiles of horizontal velocity and wind direction measured by the radiosondes at Rio Grande are shown in Fig. 9. A ninth-order polynomial was fitted to the data of the ascending sondes in order to reveal the background wind conditions and to fill gaps in the data caused by poor signal reception. Surface winds at Rio Grande were mainly around $10\text{--}15\text{ m s}^{-1}$ (Fig. 9a) with varying westerly to southerly wind direction (Fig. 9b). Wind direction in the low and midstratosphere was also mainly westerly to southwesterly and wind speed significantly decreased from around $40\text{--}60\text{ m s}^{-1}$ to almost zero at 30-km altitude after 20 September. These findings for the stratospheric winds are in agreement with the ERA5 data for the upstream region presented in Fig. 4. Fluctuations in the stratospheric horizontal wind data caused by GWs with an apparent vertical wavelength smaller than 10 km were most pronounced on 25 and 26 September, i.e., during flight ST14. Peaks in the wavelet power spectra of these profiles are found at an apparent vertical wavelength of around 5 km (not shown).

Table 3 provides a list of all GW flights, their date, length, research objectives, and summarizes the specific phenomena observed during the flights.

Figure 10 gives an overview of the vertical energy fluxes derived from the BAHAMAS in situ measurements at flight level for all straight flight legs of the GW flights (with a maximum length of 2,300 km at flight levels between 10 and 14 km). For the analysis the legs were divided into sublegs with typical lengths of ~ 300 km and then analyzed following the procedure described in Bramberger et al. (2017) which also provides a discussion of important assumptions and restrictions of such an analysis. Except for one leg all energy fluxes are positive indicating predominant upward GW propagation. The fluxes vary between 0 and 25 W m^{-2} , which is similar to the range of MW-induced energy fluxes reported by Smith et al. (2016) from measurements during DEEPWAVE.

As an example for the very different atmospheric conditions before and after the SSW we contrast ALIMA observations from flights ST08 and ST12. In Figs. 11 and 12, the altitude versus time diagrams of both observed temperatures and temperature perturbations clearly show that GW were able to propagate deeply into the mesosphere during ST08 but reached a critical level already at 40 km during ST12 as expected from our analysis of horizontal winds in Fig. 4. ST12 was the flight with strongest vertical energy fluxes at flight level (see Fig. 10).

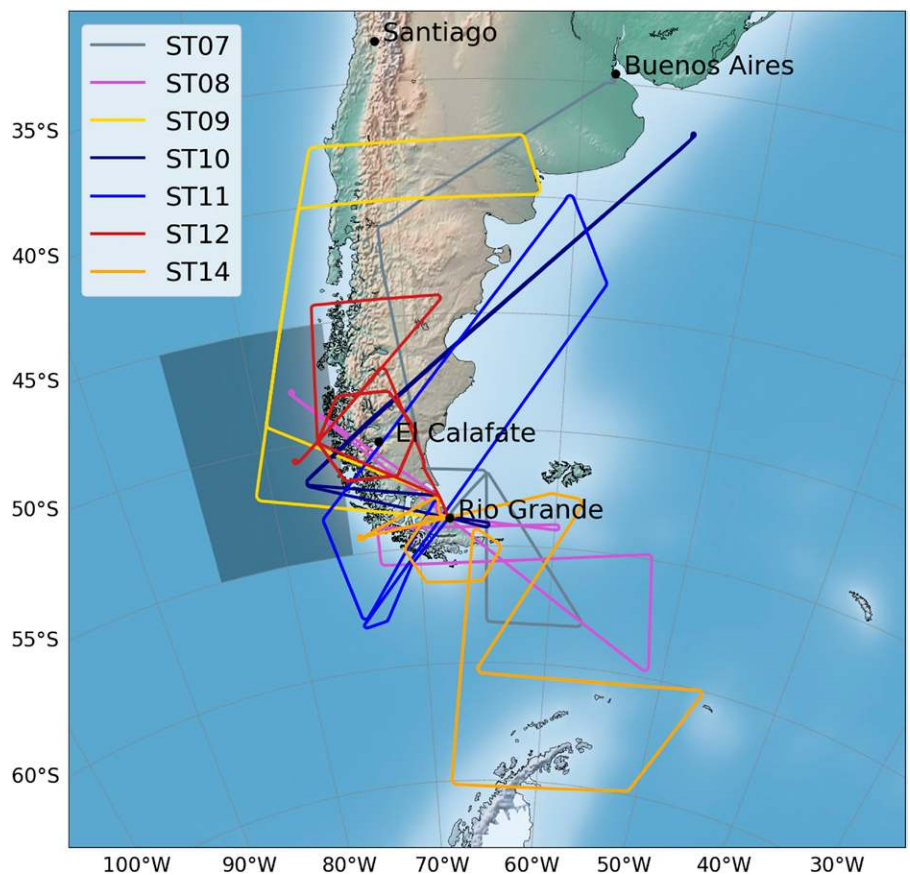


Fig. 8. Map showing the flight tracks of the seven GW flights of HALO during the SOUTHTRAC-GW mission. The typical flight distance of each flight is $\sim 7,000$ km. The gray box in the west of the tip of South America is the domain over which upstream wind profiles have been calculated (Fig. 4).

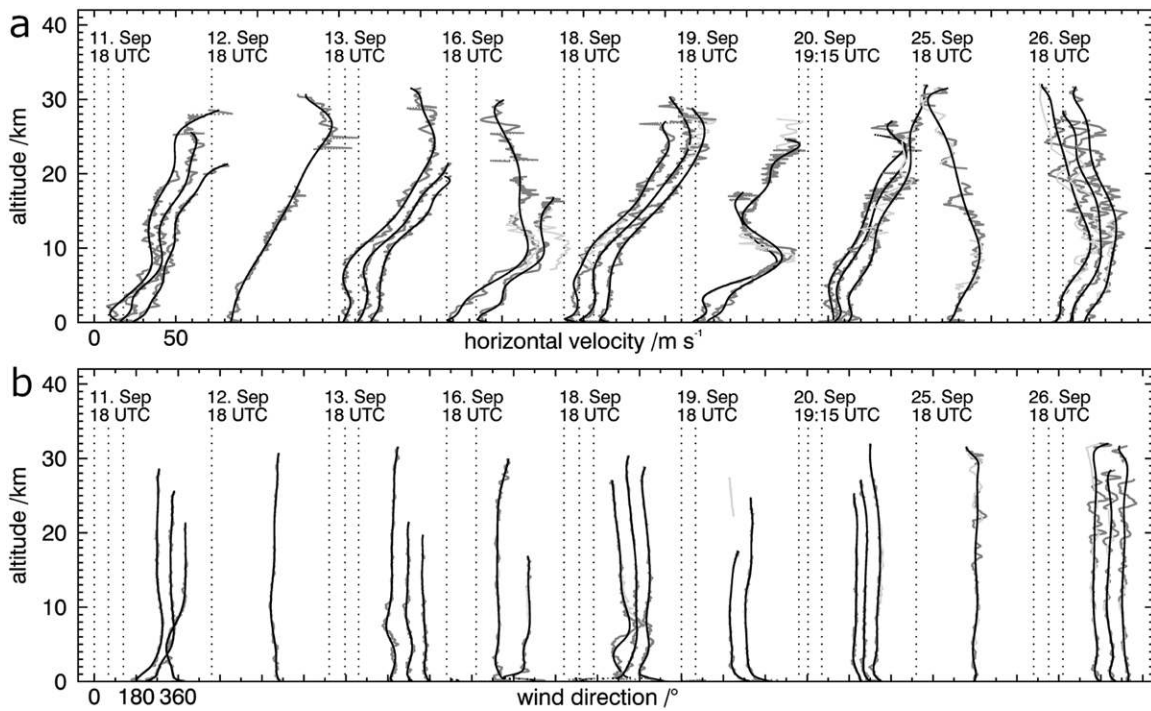


Fig. 9. Vertical profiles of (a) horizontal wind and (b) wind direction measured by the radiosondes at Rio Grande. Raw data of the ascending (descending) sondes are given in dark gray (light gray) with ninth-order polynomials fitted to the ascending data in black. The horizontal shift of the individual profiles is 9 m s^{-1} (63°) per 3-h time difference for velocity (direction) whereupon days without soundings are omitted. Vertical dotted lines mark the zero reference of the individual profiles, and the distance between ticks is 10 m s^{-1} (90°) for velocity (direction). Date and time of the first sounding are given on each day.

The observations during ST08 show several interesting features: during the cross-mountain legs of ST08 (legs 1–2 and 2–3), distinct GW phases were observed by ALIMA with very large amplitudes in excess of 10 K (maximum values are 25 K; not shown). A prominent change in vertical wavelength is observed around 40 km and again at 55-km altitude, with significantly steeper phase lines between 40 and 55 km. Preliminary analysis involving a spectral decomposition of the observations and the spatiotemporal development of the situation seen in ERA5 data suggests that this could be explained by the superposition of multiple wave modes that interact with the background wind and hence change their vertical wavelength

Table 3. SOUTHTRAC-GW flights.

Flight	Date	Start (UTC)	Length	Objectives (see Table 1)	Summary
ST07	9 Sep 2019	0700	6 h 30 min	2,3	MW, deep propagation
ST08	11/12 Sep 2019	2300	8 h 31 min	1, 2, 3, 4, 5	MW, deep propagation, breaking, secondary GWs, refraction into the PNJ and along the GW belt
ST09	13/14 Sep 2019	2300	9 h 6 min	2, 3, 5	NOGWs upstream Andes, MW
ST10	16/17 Sep 2019	2300	8 h 58 min	2, 3, 4, 5	MWs and nonorographic GW in vicinity of tropospheric jet streams, wave breaking, and effects on trace gas distributions
ST11	18/19 Sep 2019	2300	8 h 13 min	2, 3, 5	MW propagation from 40°S to jet exit region at 60°S ; PNJ edge disturbed by GWs
ST12	20/21 Sep 2019	2300	9 h 10 min	1, 2, 3, 4, 5	MW, time variation at source, refraction into the PNJ, upwind propagation, secondary GW, 3D tomography
ST14	25/26 Sep 2019	2330	9 h 17 min	1, 2, 3, 5	MW over the southern Andes and Antarctic Peninsula with weak forcing, horizontal propagation into Drake Passage, 3D tomography

(not shown). At approximately 65 km, the ALIMA measurements suggest unstable breakdown of the GW and secondary wave generation: i.e., wave amplitudes of the primary GW decrease strongly above this altitude while simultaneously occurring oppositely aligned smaller-scale phase fronts could be interpreted as features of secondary waves as discussed in N. Kaifler et al. (2017). The details of this vertical structure and the mentioned signatures for wave breaking and secondary GWs will be presented in detail in a future paper.

Further into the flight, clear GW signatures are also observed along the polar vortex at 1 hPa (leg 3–4, see also lower-left panel in Fig. 11) and in the Drake Passage (legs 4–5 and 5–6). Based on these observation and taking into account preliminary time-dependent numerical

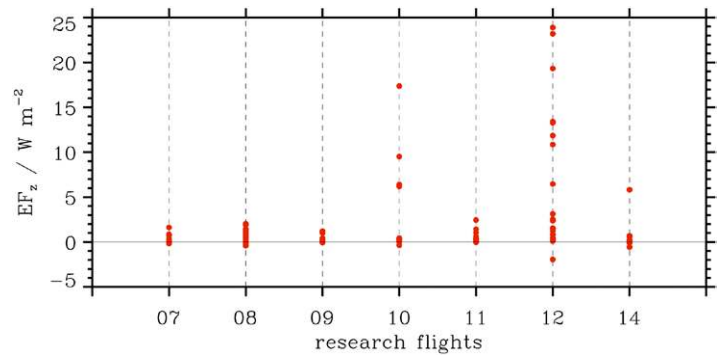


Fig. 10. Energy fluxes measured with the nose-tip probe of HALO on straight and leveled flight legs vs flight number.

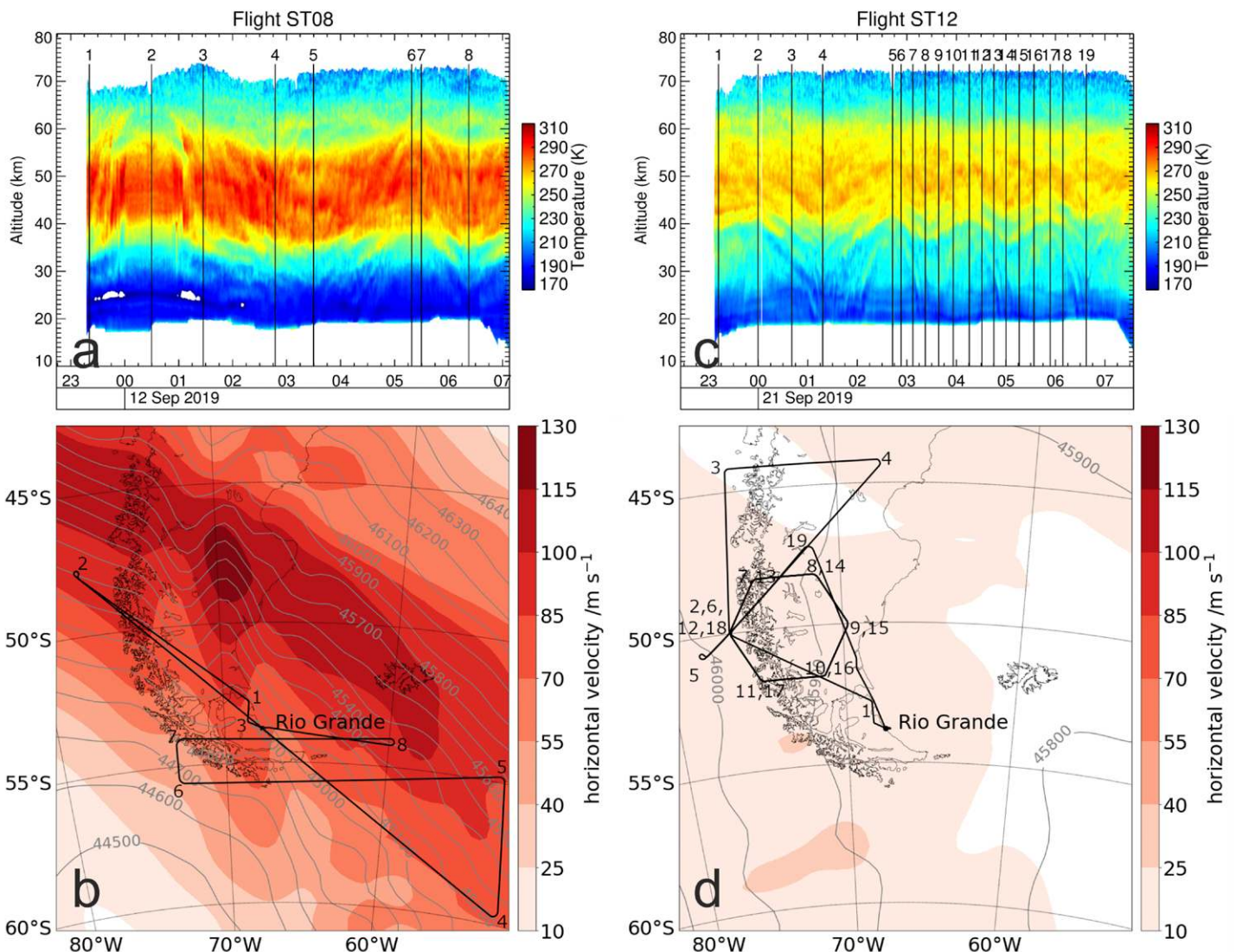


Fig. 11. (top) Contour plots of temperatures derived from ALIMA observations vs altitude and time for research flight (a) ST08 and (c) ST12; see Table 3. Vertical lines and numbers mark the start and endpoints of the flight legs. (b),(d) Corresponding flight tracks with numbers indicating the start and endpoint of flight legs with horizontal wind speeds at 1 hPa shown as colored contours in the background. Gray contour lines show isolines of geopotential height (m).

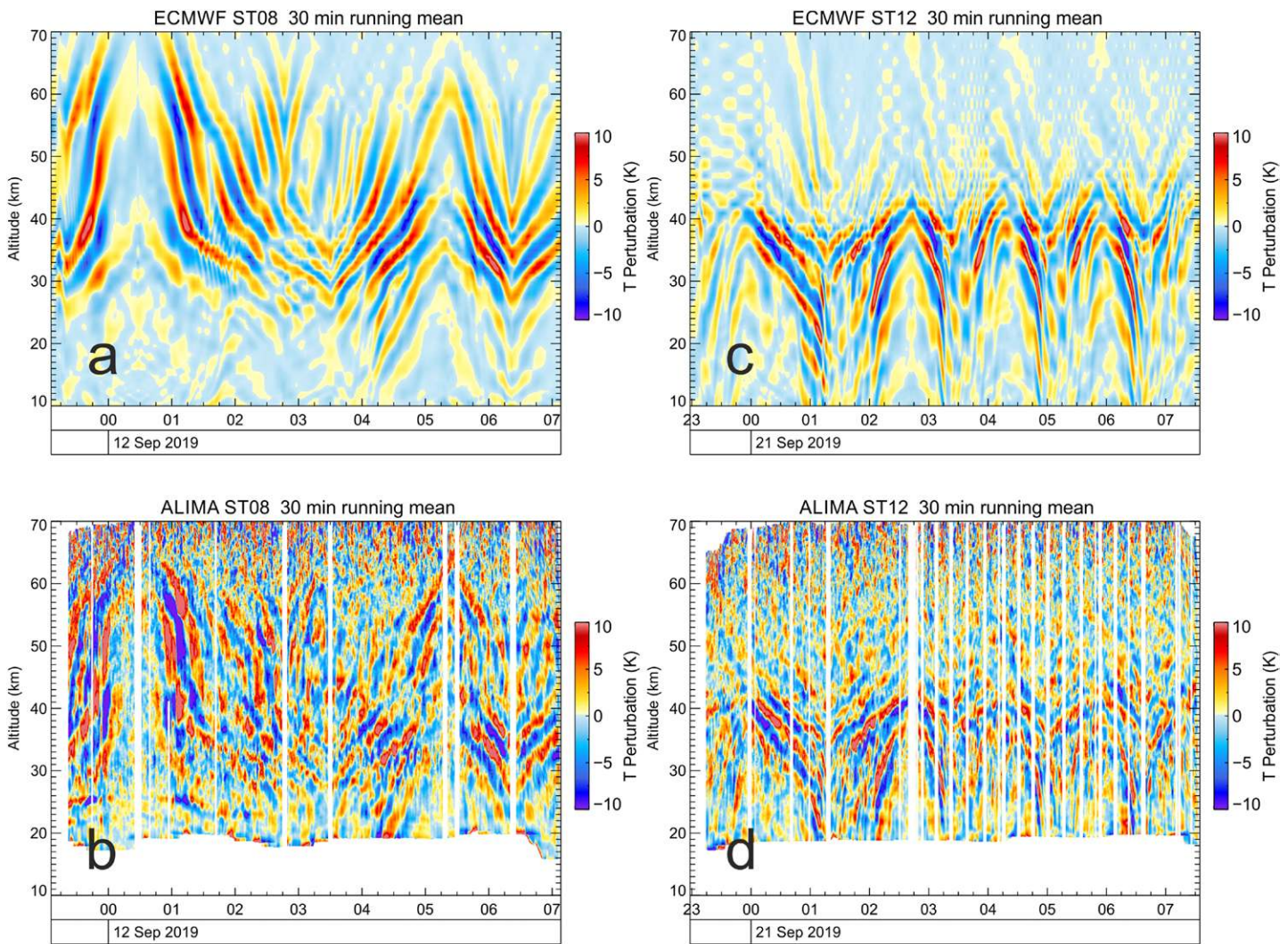


Fig. 12. (a),(c) IFS temperature perturbations compared to (b),(d) ALIMA temperature perturbations along the flight tracks of flights (left) ST08 and (right) ST12.

modeling of the situation as well as ray tracing, we hypothesize that the observed GW were excited by flow over the Andes. Subsequently, they were refracted into the PNJ and then propagated eastward in the Drake Passage toward 60°S. These high-resolution observations in time and space (in combination with yet to be completed numerical simulations) may hence provide compelling evidence that the refraction of MWs does occur in nature and is one of the sources for the GW belt as suggested by GW-resolving modeling (Sato et al. 2012), interpretation of ground based observations during DEEPWAVE (Ehard et al. 2017), and satellite observations (Hindley et al. 2019). We will test this hypothesis incorporating high-resolution three-dimensional modeling of this particular case with the Eulerian/semi-Lagrangian fluid solver (EULAG) in a future paper (see, e.g., Wilms et al. 2020, and references therein).

Figure 12 juxtaposes the ALIMA measurements during ST08 and ST12 with 1-hourly operational IFS analyses and short-term forecasts. The larger-scale features in the observations are amazingly well resolved by the IFS. Minor differences are observed with regard to exact timing, vertical extent and amplitudes of the GWs as well as smaller-scale features. Again, these are issues that will be further investigated applying high-resolution numerical modeling.

Since the IFS reproduces the gross features of the GW signatures during ST08 fairly well we may further use the model to investigate whether the model shows signatures of GW refraction

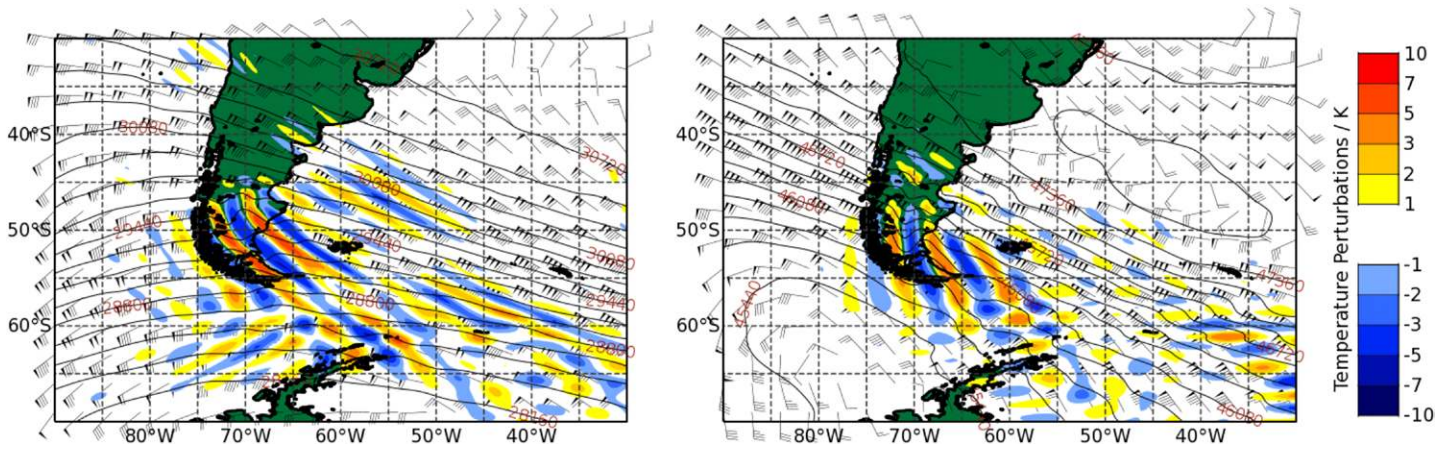


Fig. 13. ERA5 temperature perturbations $T' = T_{639} - T_{106}$ (K; color shaded in red and blue colors), geopotential height (m; solid lines), and horizontal wind (half barb = 2.5 m s^{-1} , full barb = 5 m s^{-1} , and pennant = 25 m s^{-1}) as function of latitude and longitude in the region of the southern Andes and Antarctic Peninsula during research flight ST08. ERA5 fields are shown for 0000 UTC, i.e., 1 h into the flight. Shown are (left) 10 hPa and (right) 1 hPa.

and downwind advection into the GW belt. As shown in Fig. 13, this is indeed the case: this figure shows 2D cross sections of IFS temperature perturbations, geopotential height, and horizontal winds in the region of the southern Andes and the Antarctic Peninsula at 10 and 1 hPa. At 10 hPa, those GWs that were excited both by the flow over the Andes and the Antarctic Peninsula are advected downwind and poleward. The phase fronts at 10 hPa are oriented nearly perpendicular to the westerly stratospheric wind directly above the mountains. They tilt poleward over the Drake Passage in response to the gradient of the zonal wind. At 1 hPa the wind has turned to northwesterlies and also the phase fronts have rotated into the wind, hence providing evidence for wave refraction. However, due to the weaker winds in the polar vortex, the GW cannot propagate as far poleward as at lower levels. Hence, the good agreement between observations and IFS model and the clear signature for MW propagation into the GW belt make a strong case for refraction and downwind advection

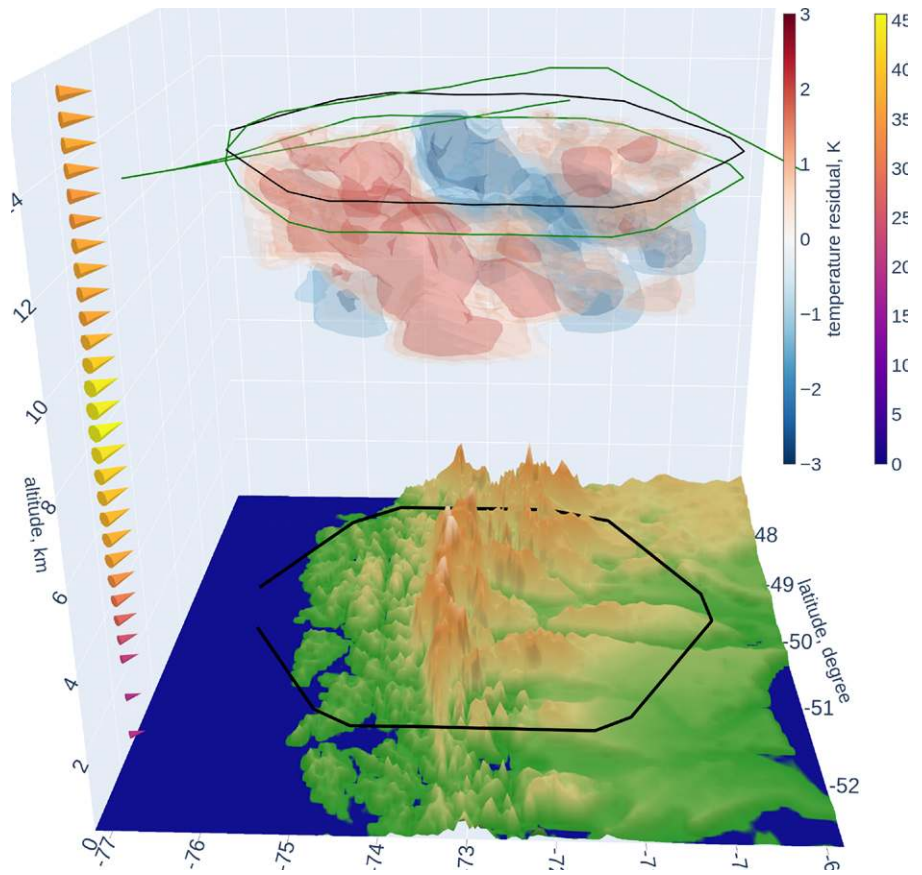


Fig. 14. A 3D tomographic retrieval of GWs observed with GLORIA during flight ST12 on 19 Sep 2019 is shown by means of isosurfaces. Thin lines show the flight path: black—the hexagonal flight path used for the depicted 3D retrieval; green—the remainder of the flight. The thick black line is the ground track of the hexagonal flight pattern. The cones show the IFS upstream wind profile.

contributing to the formation of the GW belt in support of earlier studies (Sato et al. 2012; Ehard et al. 2017; Hindley et al. 2019).

As a further initial highlight of our observations, we turn to the tomographic analysis of GLORIA measurements from the second hexagon of flight ST12. On 20 September, strong southwesterly winds in the lower troposphere ($>10 \text{ m s}^{-1}$) generated a MW over the Andes (Fig. 14). The maximum amplitude was forecasted in the area about one flight hour from Rio Grande, providing an opportunity to spend several hours in the target region and, in particular, to encircle the investigated air volume twice by a hexagonal flight pattern with a diameter of $\sim 350 \text{ km}$. Below flight level the 3D temperature structure was inferred from the infrared emissions measured by GLORIA by applying a tomographic retrieval (Ungermann et al. 2011; Krisch et al. 2017). The largest MW amplitudes were seen directly above the Andes in the western half of the hexagon. As expected for MWs, their phase fronts were oriented under a slight angle with respect to the mountain ridge and tilted southwestward, against the wind. Given the measurement setup, this GW event provides an excellent case for studying the excitation and propagation of the waves in the upper troposphere/lower stratosphere. Propagation to higher altitudes and dissipation at 40-km altitude (as suggested by the strongly decreased amplitudes above this altitude) was observed by ALIMA (Fig. 11). Thus, the combination of the two remote sensing instruments can be used to characterize the GW dynamics over almost the entire depth of the atmosphere.

Finally, we also present an example of a Stemme glider flight to illustrate the type of data and scientific potential of these measurements (Fig. 15). An overview of these

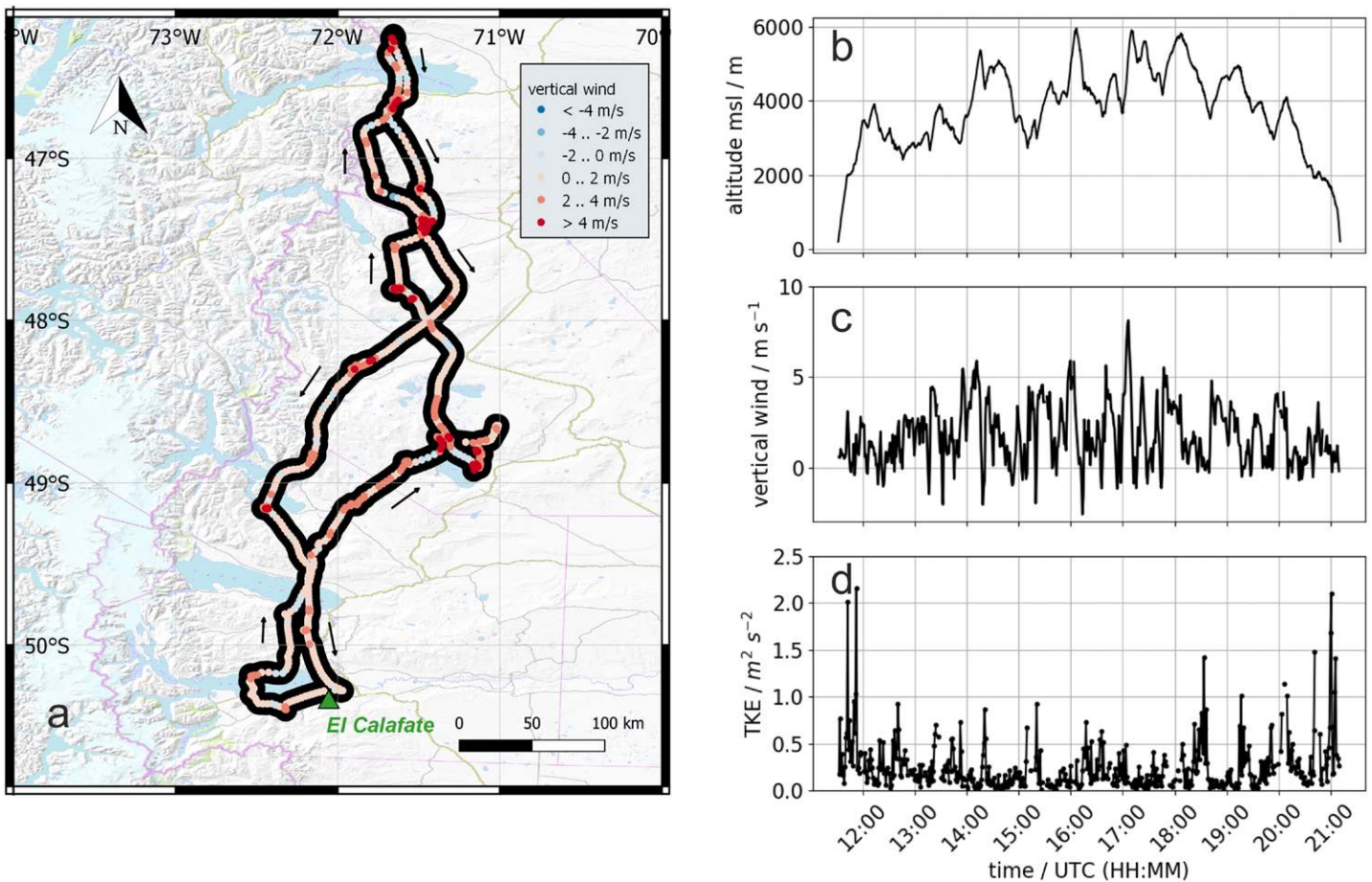


Fig. 15. (a) Flight track of the Stemme glider on 14 Sep 2019. Map data © OpenStreetMap-Contributors, SRTM; map: © OpenTopoMap (CC-BY-SA). (right) Corresponding time series of (b) flight altitude, (c) vertical wind, and (d) turbulent kinetic energy measured along the flight track.

measurements is presented in Wildmann et al. (2021). Figure 15a presents the flight track of one long-distance soaring flight from El Calafate and back as flown on 14 September 2019. Figure 15b shows the corresponding altitude profile. In search for the strongest updrafts the Stemme climbed several times in the ascending branches of mountain lee waves. Hence, the observations were not conducted at a fixed altitude like during HALO flights but are taken along a sawtooth pattern. Correspondingly, the scientific interpretation of these data will need to take the motion of this measurement platform into account. An example for such measurements is the vertical wind and turbulence kinetic energy data (derived from high-resolution wind measurements with the 5-hole probe mounted under the wings of the glider; see Wildmann et al. 2021), which are also shown in Figs. 15c and 15d, respectively. It shows that in periods of soaring in the updraft of the waves, high vertical velocity (up to 8 m s^{-1}) and low turbulence prevails, whereas higher turbulence is detected in phases of the flight when the glider was outside the updraft branch of the waves (low vertical velocity and descending altitude). Despite the complication of changing flight altitudes, this dataset will be used to investigate tropospheric lee waves and to evaluate numerical weather prediction models. For a single case study, Wildmann et al. (2021) show that these measurements compare well to the predictions of a mesoscale model at 1-km horizontal resolution, but differences remain between modeled and observed magnitude of vertical velocities and the locations of the waves.

Summary and outlook

SOUTHTRAC-GW was the first airborne field campaign targeting GW dynamics in the atmosphere from the troposphere up to the mesopause region at the world's strongest stratospheric GW hotspot, i.e., the region of the southern Andes and the Antarctic Peninsula. One transfer flight from Buenos Aires and six research flights from Rio Grande, Argentina, were conducted with the German research aircraft HALO in September 2019 each covering a distance of about 7,000 km. The total number of flight hours was 59.75. During these flights a comprehensive instrument package of remote and in situ instruments allowed us to characterize GWs from 5- to 80-km altitude. The campaign period coincided with the occurrence of a rare SSW which created a critical level for stationary MWs at about 40-km altitude after 13 September with pronounced effects on subsequent GW propagation and corresponding mesospheric temperatures and winds. Two of the research flights were conducted before and five after the occurrence of the stationary wave critical level at 40 km. Hence, SOUTHTRAC-GW succeeded to take measurements both during conditions of deep GW propagation into the upper mesosphere and during conditions where GWs encountered wave breaking and dissipation already at or below 40-km altitude. Thus, the September 2019 period may be considered as a condensed period of the transition from a winter to a summer regime and allowed us to take observations during both atmospheric states within a short period of time.

Preliminary analysis of our measurements and accompanying model results reveal strong evidence for MW excitation over the Andes and subsequent vertical as well as horizontal propagation including refraction and downwind advection into the PNJ and along the GW belt. Our findings strongly suggest that these processes are one of the reasons for the early development of the GW belt in the vicinity of the southern Andes and Antarctic Peninsula. More detailed numerical modeling and data analysis (including ray tracing) will be conducted in the coming months to corroborate these preliminary observational results. In addition, during two of our research flights we were able to comprehensively characterize the full 3D structure of upper tropospheric GWs excited over the Andes. Further analysis will yield unprecedented details of the properties of such waves. The remote sensing measurements by ALIMA and GLORIA will hence be a benchmark dataset for future high-resolution modeling.

Also a clear-cut case with MW excitation over the Antarctic peninsula was characterized by airborne measurements. Furthermore, several of the research flights reveal indications of GW breaking and secondary wave excitation as indicated by corresponding scales and spatiotemporal morphologies of observed phase fronts (N. Kaifler et al. 2017). Secondary wave excitation is an exciting topic (Becker and Vadas 2018) which remains very difficult to probe and for which numerical simulations require enormous efforts (e.g., Dong et al. 2020). Hence, these data have the potential to serve as an invaluable guidance for high-resolution modeling of such processes and will allow us to yield a deeper understanding of the corresponding fundamental dynamics of GWs.

In the coming months, the preliminary results mentioned above will be further scrutinized including dedicated efforts of high-resolution modeling, and including additional data sources like from satellite instruments like AIRS (e.g., Hindley et al. 2019). In addition, we will consider in how far the results obtained from combined observations and modeling will be useful for the important challenge of formulating improved gravity wave parameterizations for climate models (Plougonven et al. 2020). Furthermore, improvements of the ALIMA instrument to incorporate an iron resonance lidar channel (B. Kaifler et al. 2017) are under way which will extend the measurement range of ALIMA to 110 km and also add the ability to measure vertical winds. With these instrumental improvements, a follow-up airborne mission is currently being planned for Northern Hemisphere winter 2021 during which the same set of instruments on HALO will be utilized to further characterize the role of the polar vortex for GW propagation and its impact on the middle atmosphere circulation.

Acknowledgments. The authors gratefully acknowledge the enormous hospitality of the Argentinian Navy who hosted HALO and our team in their facilities at the Naval air base of Rio Grande. We also thank the Argentinian and Chilean authorities for their permission to perform research flights in their airspace. Thanks also for excellent support by the DLR facility for Flight Experiments (FX) and Klaus Ohlmann, the ingenious pilot of the Stemme glider. We are grateful for Annelize van Niekerk (UK MetOffice) for providing the Unified Model simulations applied during flight planning of HALO flights. The National Meteorological Service of Argentina (SMN) and the German Weather Service (DWD) supported the SOUTHTRAC-GW campaign by providing regional forecasts. Alejandro Godoy, Nicolas Rivaben (SMN) and Tobias Göcke (DWD) participated in the forecast team. Collaboration with AvN was established in the framework of the ISSI Team “New Quantitative Constraints on OGW Stress and Drag” at the ISSI Bern. This work was partly funded by the Federal Ministry for Education and Research under Grants 01LG1907 (project WASCLIM) in the frame of the Role of the Middle Atmosphere in Climate (ROMIC) program as well as by internal funds of the German Aerospace Center, the Karlsruhe Institute of Technology, and Forschungszentrum Jülich. The university groups involved were funded by the German Science Foundation (DFG) through the HALO-SPP. Further support by the German Science foundation under Grants GW-TP/DO1020/9-1 and PACOG/RA1400/6-1 in the frame of the DFG research group MS-GWAVES (FOR1898) is also acknowledged. Access to ECMWF data was granted through the special project “Deep Vertical Propagation of Internal Gravity Waves.”

Data availability statement. Airborne, CORAL, and radiosonde data can be accessed via the HALO database under <https://halo-db.pa.op.dlr.de>. According to HALO data policy, data are freely available from 30 months after the end of the mission, i.e., from June 2022. Before this date, data shown in this publication are available from the first author upon request. IFS forecast and ERA5-data data can be found under www.ecmwf.int/en/forecasts/datasets/set-i and www.ecmwf.int/en/forecasts/datasets/reanalysis-datasets/era5, respectively. MetOp RO data are available from www.romsaf.org. SAAMER data can be downloaded from the Madrigal database under <http://millstonehill.haystack.mit.edu>. SABER data are available at <http://saber.gats-inc.com>.

References

- Alexander, M. J., and A. W. Grimsdell, 2013: Seasonal cycle of orographic gravity wave occurrence above small islands in the Southern Hemisphere: Implications for effects on the general circulation. *J. Geophys. Res. Atmos.*, **118**, 11 589–11 599, <https://doi.org/10.1002/2013JD020526>.
- , S. D. Eckermann, D. Broutman, and J. Ma, 2009: Momentum flux estimates for South Georgia Island mountain waves in the stratosphere observed via satellite. *Geophys. Res. Lett.*, **36**, L12816, <https://doi.org/10.1029/2009GL038587>.
- , and Coauthors, 2010: Recent developments in gravity-wave effects in climate models and the global distribution of gravity-wave momentum flux from observations and models. *Quart. J. Roy. Meteor. Soc.*, **136**, 1103–1124, <https://doi.org/10.1002/qj.637>.
- Alexander, P., D. Luna, P. Llamedo, and A. de la Torre, 2010: A gravity waves study close to the Andes Mountains in Patagonia and Antarctica with GPS radio occultation observations. *Ann. Geophys.*, **28**, 587–595, <https://doi.org/10.5194/angeo-28-587-2010>.
- , A. de la Torre, N. Kaifler, B. Kaifler, J. Salvador, P. Llamedo, R. Hierro, and J. L. Hormaechea, 2020: Temperature profiles from two close lidars and a satellite to infer the structure of a dominant gravity wave. *Earth Space Sci.*, **7**, e2020EA001074, <https://doi.org/10.1029/2020EA001074>.
- Austin, J., and Coauthors, 2003: Uncertainties and assessments of chemistry-climate models of the stratosphere. *Atmos. Chem. Phys.*, **3**, 1–27, <https://doi.org/10.5194/acp-3-1-2003>.
- Becker, E., and S. L. Vadas, 2018: Secondary gravity waves in the winter mesosphere: Results from a high-resolution global circulation model. *J. Geophys. Res. Atmos.*, **123**, 2605–2627, <https://doi.org/10.1002/2017JD027460>.
- Bossert, K., C. G. Kruse, C. J. Heale, D. C. Fritts, B. P. Williams, J. B. Snively, P.-D. Pautet, and M. J. Taylor, 2017: Secondary gravity wave generation over New Zealand during the DEEPWAVE campaign. *J. Geophys. Res. Atmos.*, **122**, 7834–7850, <https://doi.org/10.1002/2016JD026079>.
- , and Coauthors, 2018: Momentum flux spectra of a mountain wave event over New Zealand. *J. Geophys. Res. Atmos.*, **123**, 9980–9991, <https://doi.org/10.1029/2018JD028319>.
- Bramberger, M., and Coauthors, 2017: Does strong tropospheric forcing cause large-amplitude mesospheric gravity waves? A DEEPWAVE case study. *J. Geophys. Res. Atmos.*, **122**, 11 422–11 443, <https://doi.org/10.1002/2017JD027371>.
- , A. Dörnbrack, H. Wilms, F. Ewald, and R. Sharman, 2020: Mountain-wave turbulence encounter of the research aircraft HALO above Iceland. *J. Appl. Meteor. Climatol.*, **59**, 567–588, <https://doi.org/10.1175/JAMC-D-19-0079.1>.
- Bruzzone, J. S., D. Janches, P. Jenniskens, R. Weryk, and J. L. Hormaechea, 2020: A comparative study of radar and optical observations of meteor showers using SAAMER-OS and CAMS. *Planet. Space Sci.*, **188**, 104936, <https://doi.org/10.1016/j.pss.2020.104936>.
- Butchart, N., and Coauthors, 2011: Multimodel climate and variability of the stratosphere. *J. Geophys. Res.*, **116**, D05102, <https://doi.org/10.1029/2010JD014995>.
- Cámara, A., F. Lott, V. Jewtoukoff, R. Plougonven, and A. Hertzog, 2016: On the gravity wave forcing during the southern stratospheric final warming in LMDZ. *J. Atmos. Sci.*, **73**, 3213–3226, <https://doi.org/10.1175/JAS-D-15-0377.1>.
- Chau, J. L., G. Stober, C. M. Hall, M. Tsutsumi, F. I. Laskar, and P. Hoffmann, 2017: Polar mesospheric horizontal divergence and relative vorticity measurements using multiple specular meteor radars. *Radio Sci.*, **52**, 811–828, <https://doi.org/10.1002/2016RS006225>.
- , and Coauthors, 2020: Multistatic specular meteor radar network in Peru: System description and initial results. *Earth Space Sci.*, **29**, e2020EA001293, <https://doi.org/10.1002/essoar.10503328.1>.
- Choi, H.-J., and H.-Y. Chun, 2013: Effects of convective gravity wave drag in the Southern Hemisphere winter stratosphere. *J. Atmos. Sci.*, **70**, 2120–2136, <https://doi.org/10.1175/JAS-D-12-0238.1>.
- de la Torre, A., P. Alexander, R. Hierro, P. Llamedo, A. Rolla, T. Schmidt, and J. Wickert, 2012: Large-amplitude gravity waves above the southern Andes, the Drake Passage, and the Antarctic Peninsula. *J. Geophys. Res.*, **117**, D02106, <https://doi.org/10.1029/2011JD016377>.
- de Wit, R. J., D. Janches, D. C. Fritts, R. G. Stockwell, and L. Coy, 2017: Unexpected climatological behavior of MLT gravity wave momentum flux in the lee of the southern Andes hot spot. *Geophys. Res. Lett.*, **44**, 1182–1191, <https://doi.org/10.1002/2016GL072311>.
- Dong, W., D. C. Fritts, T. S. Lund, S. A. Wieland, and S. Zhang, 2020: Self-acceleration and instability of gravity wave packets: 2. Two-dimensional packet propagation, instability dynamics, and transient flow responses. *J. Geophys. Res. Atmos.*, **125**, e2019JD030691, <https://doi.org/10.1029/2019JD030691>.
- Dörnbrack, A., and Coauthors, 2020: Unusual appearance of mother-of-pearl clouds above El Calafate, Argentina. *Weather*, **75**, 378–388, <https://doi.org/10.1002/wea.3863>.
- Dunkerton, T., 1984: Inertia-gravity waves in the stratosphere. *J. Atmos. Sci.*, **41**, 3396–3404, [https://doi.org/10.1175/1520-0469\(1984\)041<3396:IWITS>2.0.CO;2](https://doi.org/10.1175/1520-0469(1984)041<3396:IWITS>2.0.CO;2).
- Eckermann, S. D., and Coauthors, 2016: Dynamics of orographic gravity waves observed in the mesosphere over the Auckland islands during the Deep Propagating Gravity Wave Experiment (DEEPWAVE). *J. Atmos. Sci.*, **73**, 3855–3876, <https://doi.org/10.1175/JAS-D-16-0059.1>.
- Ehard, B., and Coauthors, 2017: Horizontal propagation of large-amplitude mountain waves into the polar night jet. *J. Geophys. Res. Atmos.*, **122**, 1423–1436, <https://doi.org/10.1002/2016JD025621>.
- , S. Malardel, A. Dörnbrack, B. Kaifler, N. Kaifler, and N. Wedi, 2018: Comparing ECMWF high-resolution analyses with lidar temperature measurements in the middle atmosphere. *Quart. J. Roy. Meteor. Soc.*, **144**, 633–640, <https://doi.org/10.1002/qj.3206>.
- Ern, M., P. Preusse, and C. D. Warner, 2006: Some experimental constraints for spectral parameters used in the Warner and McIntyre gravity wave parameterization scheme. *Atmos. Chem. Phys.*, **6**, 4361–4381, <https://doi.org/10.5194/acp-6-4361-2006>.
- , Q. T. Trinh, P. Preusse, J. C. Gille, M. G. Mlynarczyk, J. M. Russell III, and M. Riese, 2018: GRACILE: A comprehensive climatology of atmospheric gravity wave parameters based on satellite limb soundings. *Earth Syst. Sci. Data*, **10**, 857–892, <https://doi.org/10.5194/essd-10-857-2018>.
- Friedl-Vallon, F., and Coauthors, 2014: Instrument concept of the imaging Fourier transform spectrometer GLORIA. *Atmos. Meas. Tech.*, **7**, 3565–3577, <https://doi.org/10.5194/amt-7-3565-2014>.
- Fritts, D. C., and M. J. Alexander, 2003: Gravity wave dynamics and effects in the middle atmosphere. *Rev. Geophys.*, **41**, 1003, <https://doi.org/10.1029/2001RG000106>.
- , D. Janches, and W. K. Hocking, 2010a: Southern Argentina Agile Meteor Radar: Initial assessment of gravity wave momentum fluxes. *J. Geophys. Res.*, **115**, D19123, <https://doi.org/10.1029/2010JD013891>.
- , and Coauthors, 2010b: Southern Argentina Agile Meteor Radar: System design and initial measurements of large-scale winds and tides. *J. Geophys. Res.*, **115**, D18112, <https://doi.org/10.1029/2010JD013850>.
- , and Coauthors, 2016: The Deep Propagating Gravity Wave Experiment (DEEPWAVE): An airborne and ground-based exploration of gravity wave propagation and effects from their sources throughout the lower and middle atmosphere. *Bull. Amer. Meteor. Soc.*, **97**, 425–453, <https://doi.org/10.1175/BAMS-D-14-00269.1>.
- , and Coauthors, 2018: Large-amplitude mountain waves in the mesosphere accompanying weak cross-mountain flow during DEEPWAVE research flight RF22. *J. Geophys. Res. Atmos.*, **123**, 9992–10 022, <https://doi.org/10.1029/2017JD028250>.
- García, R. R., A. K. Smith, D. E. Kinnison, Á. de la Cámara, and D. J. Murphy, 2017: Modification of the gravity wave parameterization in the Whole Atmosphere Community Climate Model: Motivation and results. *J. Atmos. Sci.*, **74**, 275–291, <https://doi.org/10.1175/JAS-D-16-0104.1>.
- Geller, M. A., and Coauthors, 2013: A comparison between gravity wave momentum fluxes in observations and climate models. *J. Climate*, **26**, 6383–6405, <https://doi.org/10.1175/JCLI-D-12-00545.1>.

- Giez, A., C. Mallaun, M. Zöger, A. Dörnbrack, and U. Schumann, 2017: Static pressure from aircraft trailing-cone measurements and numerical weather-prediction analysis. *J. Aircr.*, **54**, 1728–1737, <https://doi.org/10.2514/1.C034084>.
- , M. Zöger, V. Dreiling, and C. Mallaun, 2019: Static source error calibration of a nose boom mounted air data system on an atmospheric research aircraft using the trailing cone method. DLR Internal Rep. 2019-07, 87 pp.
- Gisinger, S., J. Wagner, and B. Witschas, 2020: Airborne measurements and large-eddy simulations of small-scale gravity waves at the tropopause inversion layer over Scandinavia. *Atmos. Chem. Phys.*, **20**, 10091–10109, <https://doi.org/10.5194/acp-20-10091-2020>.
- GRAW, 2019: GRAW radiosonde DFM-09 data sheet. GRAW Doc., 6 pp., www.graw.de/fileadmin/cms_upload/en/Resources/pdf.
- Hauchecorne, A., and M.-L. Chanin, 1980: Density and temperature profiles obtained by lidar between 35 and 70 km. *Geophys. Res. Lett.*, **7**, 565–568, <https://doi.org/10.1029/GL007i008p00565>.
- Hendricks, E. A., J. D. Doyle, S. D. Eckermann, Q. Jiang, and P. A. Reinecke, 2014: What is the source of the stratospheric gravity wave belt in austral winter? *J. Atmos. Sci.*, **71**, 1583–1592, <https://doi.org/10.1175/JAS-D-13-0332.1>.
- Hersbach, H., and Coauthors, 2020: The ERA5 global reanalysis. *Quart. J. Roy. Meteor. Soc.*, **146**, 1999–2049, <https://doi.org/10.1002/qj.3803>.
- Hindley, N. P., C. J. Wright, N. D. Smith, and N. J. Mitchell, 2015: The southern stratospheric gravity wave hot spot: Individual waves and their momentum fluxes measured by COSMIC GPS-RO. *Atmos. Chem. Phys.*, **15**, 7797–7818, <https://doi.org/10.5194/acp-15-7797-2015>.
- , ———, ———, L. Hoffmann, L. A. Holt, M. J. Alexander, T. Moffat-Griffin, and N. J. Mitchell, 2019: Gravity waves in the winter stratosphere over the Southern Ocean: High-resolution satellite observations and 3-D spectral analysis. *Atmos. Chem. Phys.*, **19**, 15377–15414, <https://doi.org/10.5194/acp-19-15377-2019>.
- Hocking, W. K., 2005: A new approach to momentum flux determinations using SKIYMET meteor radars. *Ann. Geophys.*, **23**, 2433–2439, <https://doi.org/10.5194/angeo-23-2433-2005>.
- Hoffmann, L., X. Xue, and M. J. Alexander, 2013: A global view of stratospheric gravity wave hotspots located with Atmospheric Infrared Sounder observations. *J. Geophys. Res. Atmos.*, **118**, 416–434, <https://doi.org/10.1029/2012JD018658>.
- Hoffmann, P., W. Singer, and D. Keuer, 2002: Variability of the mesospheric wind field at middle and arctic latitudes in winter and its relation to stratospheric circulation disturbances. *J. Atmos. Sol.-Terr. Phys.*, **64**, 1229–1240, [https://doi.org/10.1016/S1364-6826\(02\)00071-8](https://doi.org/10.1016/S1364-6826(02)00071-8).
- Holt, L. A., M. J. Alexander, L. Coy, C. Liu, A. Molod, W. Putman, and S. Pawson, 2017: An evaluation of gravity waves and gravity wave sources in the Southern Hemisphere in a 7 km global climate simulation. *Quart. J. Roy. Meteor. Soc.*, **143**, 2481–2495, <https://doi.org/10.1002/qj.3101>.
- Janches, D., and Coauthors, 2015: The Southern Argentina Agile Meteor Radar Orbital System (SAAMER-OS): An initial sporadic meteoroid orbital survey in the southern sky. *Astrophys. J.*, **809**, 36, <https://doi.org/10.1088/0004-637X/809/1/36>.
- , J. S. Bruzzone, R. J. Weryk, J. L. Hormaechea, P. Wiegert, and C. Brunini, 2020: Observations of an unexpected meteor shower outburst at high ecliptic southern latitude and its potential origin. *Astrophys. J.*, **895**, L25, <https://doi.org/10.3847/2041-8213/ab9181>.
- Jiang, Q., J. D. Doyle, S. D. Eckermann, and B. P. Williams, 2019: Stratospheric trailing gravity waves from New Zealand. *J. Atmos. Sci.*, **76**, 1565–1586, <https://doi.org/10.1175/JAS-D-18-0290.1>.
- Kaifler, B., and N. Kaifler, 2020: A Compact Rayleigh Autonomous Lidar (CORAL) for the middle atmosphere. *Atmos. Meas. Tech.*, **2020**, 1–24, <https://doi.org/10.5194/amt-2020-418>.
- , ———, B. Ehard, A. Dörnbrack, M. Rapp, and D. C. Fritts, 2015: Influences of source conditions on mountain wave penetration into the stratosphere and mesosphere. *Geophys. Res. Lett.*, **42**, 9488–9494, <https://doi.org/10.1002/2015GL066465>.
- , C. Büdenbender, P. Mahnke, M. Damm, D. Sauder, N. Kaifler, and M. Rapp, 2017: Demonstration of an iron fluorescence lidar operating at 372 nm wavelength using a newly-developed Nd:YAG laser. *Opt. Lett.*, **42**, 2858–2861, <https://doi.org/10.1364/OL.42.002858>.
- Kaifler, N., and Coauthors, 2017: Observational indications of downward-propagating gravity waves in middle atmosphere lidar data. *J. Atmos. Sol.-Terr. Phys.*, **162**, 16–27, <https://doi.org/10.1016/j.jastp.2017.03.003>.
- , B. Kaifler, A. Dörnbrack, M. Rapp, J. L. Hormaechea, and A. de la Torre, 2020: Lidar observations of large-amplitude mountain waves in the stratosphere above Tierra del Fuego, Argentina. *Sci. Rep.*, **10**, 14529, <https://doi.org/10.1038/s41598-020-71443-7>.
- Kaufmann, M., and Coauthors, 2015: Retrieval of three-dimensional small-scale structures in upper-tropospheric/lower-stratospheric composition as measured by GLORIA. *Atmos. Meas. Tech.*, **8**, 81–95, <https://doi.org/10.5194/amt-8-81-2015>.
- Krautstrunk, M., and A. Giez, 2012: The transition from FALCON to HALO era airborne atmospheric research. *Atmospheric Physics*, U. Schumann, Ed., Springer, 609–624.
- Krisch, I., and Coauthors, 2017: First tomographic observations of gravity waves by the infrared limb imager GLORIA. *Atmos. Chem. Phys.*, **17**, 14937–14953, <https://doi.org/10.5194/acp-17-14937-2017>.
- , J. Ungermann, P. Preusse, E. Kretschmer, and M. Riese, 2018: Limited angle tomography of mesoscale gravity waves by the infrared limb-sounder GLORIA. *Atmos. Meas. Tech.*, **11**, 4327–4344, <https://doi.org/10.5194/amt-11-4327-2018>.
- , M. Ern, L. Hoffmann, P. Preusse, C. Strube, J. Ungermann, W. Woiwode, and M. Riese, 2020: Superposition of gravity waves with different propagation characteristics observed by airborne and space-borne infrared sounders. *Atmos. Chem. Phys.*, **20**, 11469–11490, <https://doi.org/10.5194/acp-20-11469-2020>.
- Kruse, C. G., R. B. Smith, and S. D. Eckermann, 2016: The midlatitude lower-stratospheric mountain wave “valve layer.” *J. Atmos. Sci.*, **73**, 5081–5100, <https://doi.org/10.1175/JAS-D-16-0173.1>.
- Kunkel, D., and Coauthors, 2019: Evidence of small-scale quasi-isentropic mixing in ridges of extratropical baroclinic waves. *Atmos. Chem. Phys.*, **19**, 12607–12630, <https://doi.org/10.5194/acp-19-12607-2019>.
- Limpasuvan, V., Y. J. Orsolini, A. Chandran, R. R. Garcia, and A. K. Smith, 2016: On the composite response of the MLT to major sudden stratospheric warming events with elevated stratopause. *J. Geophys. Res. Atmos.*, **121**, 4518–4537, <https://doi.org/10.1002/2015JD024401>.
- Lin, E. P., and Coauthors, 2020: The 2019 Antarctic sudden stratospheric warming. *SPARC Newsletter*, No. 54, DLR, Oberpfaffenhofen, Germany, 10–13.
- Llamedo, P., and Coauthors, 2019: 11 years of Rayleigh lidar observations of gravity wave activity above the southern tip of South America. *J. Geophys. Res. Atmos.*, **124**, 451–467, <https://doi.org/10.1029/2018JD028673>.
- McLandsess, C., and T. G. Shepherd, 2009: Simulated anthropogenic changes in the Brewer–Dobson circulation, including its extension to high latitudes. *J. Climate*, **22**, 1516–1540, <https://doi.org/10.1175/2008JCLI2679.1>.
- , ———, S. Polavarapu, and S. R. Beagley, 2012: Is missing orographic gravity wave drag near 60°S the cause of the stratospheric zonal wind biases in chemistry–climate models? *J. Atmos. Sci.*, **69**, 802–818, <https://doi.org/10.1175/JAS-D-11-0159.1>.
- Oelhof, H., and Coauthors, 2020: POLSTRACC: Airborne experiment for studying the polar stratosphere in a changing climate with the High Altitude and Long Range Research Aircraft (HALO). *Bull. Amer. Meteor. Soc.*, **100**, 2634–2664, <https://doi.org/10.1175/BAMS-D-18-0181.1>.
- Pautet, P.-D., and Coauthors, 2016: Large-amplitude mesospheric response to an orographic wave generated over the Southern Ocean Auckland Islands (50.7°S) during the DEEPWAVE project. *J. Geophys. Res. Atmos.*, **121**, 1431–1441, <https://doi.org/10.1002/2015JD024336>.
- , M. J. Taylor, S. D. Eckermann, and N. Criddle, 2019: Regional distribution of mesospheric small-scale gravity waves during DEEPWAVE. *J. Geophys. Res. Atmos.*, **124**, 7069–7081, <https://doi.org/10.1029/2019JD030271>.
- Plougonven, R., and F. Zhang, 2014: Internal gravity waves from atmospheric jets and fronts. *Rev. Geophys.*, **52**, 33–76, <https://doi.org/10.1002/2012RG000419>.

- , A. Hertzog, and M. J. Alexander, 2015: Case studies of nonorographic gravity waves over the Southern Ocean emphasize the role of moisture. *J. Geophys. Res. Atmos.*, **120**, 1278–1299, <https://doi.org/10.1002/2014JD022332>.
- , A. de la Cámara, A. Hertzog, and F. Lott, 2020: How does knowledge of atmospheric gravity waves guide their parameterizations? *Quart. J. Roy. Meteor. Soc.*, **146**, 1529–1543, <https://doi.org/10.1002/qj.3732>.
- Polichtchouk, I., R. Hogan, T. Shepherd, P. Bechtold, T. Stockdale, S. Malardel, S.-J. Lock, and L. Magnusson, 2017: What influences the middle atmosphere circulation in the IFS? ECMWF Tech. Rep. 809, 50 pp., www.ecmwf.int/node/17670.
- Portele, T. C., A. Dörnbrack, J. S. Wagner, S. Gisinger, B. Ehard, P.-D. Pautet, and M. Rapp, 2018: Mountain-wave propagation under transient tropospheric forcing: A DEEPWAVE case study. *Mon. Wea. Rev.*, **146**, 1861–1888, <https://doi.org/10.1175/MWR-D-17-0080.1>.
- Preusse, P., A. Dörnbrack, S. D. Eckermann, M. Riese, B. Schaefer, J. T. Bacmeister, D. Broutman, and K. U. Grossmann, 2002: Space-based measurements of stratospheric mountain waves by CRISTA 1. Sensitivity, analysis method, and a case study. *J. Geophys. Res.*, **107**, 8178, <https://doi.org/10.1029/2001JD000699>.
- Rapp, M., A. Dörnbrack, and B. Kaifler, 2018a: An intercomparison of stratospheric gravity wave potential energy densities from MetOp GPS radio occultation measurements and ECMWF model data. *Atmos. Meas. Tech.*, **11**, 1031–1048, <https://doi.org/10.5194/amt-11-1031-2018>.
- , —, and P. Preusse, 2018b: Large midlatitude stratospheric temperature variability caused by inertial instability: A potential source of bias for gravity wave climatologies. *Geophys. Res. Lett.*, **45**, 10682–10690, <https://doi.org/10.1029/2018GL079142>.
- Reichert, R., and Coauthors, 2019: Retrieval of intrinsic mesospheric gravity wave parameters using lidar and airglow temperature and meteor radar wind data. *Atmos. Meas. Tech.*, **12**, 5997–6015, <https://doi.org/10.5194/amt-12-5997-2019>.
- Remsberg, E. E., and Coauthors, 2008: Assessment of the quality of the version 1.07 temperature-versus-pressure profiles of the middle atmosphere from timed/saber. *J. Geophys. Res.*, **113**, D17101, <https://doi.org/10.1029/2008JD010013>.
- Riese, M., and Coauthors, 2014: Gimballed Limb Observer for Radiance Imaging of the Atmosphere (GLORIA) scientific objectives. *Atmos. Meas. Tech.*, **7**, 1915–1928, <https://doi.org/10.5194/amt-7-1915-2014>.
- Sato, K., and M. Yoshiki, 2008: Gravity wave generation around the polar vortex in the stratosphere revealed by 3-hourly radiosonde observations at Syowa station. *J. Atmos. Sci.*, **65**, 3719–3735, <https://doi.org/10.1175/2008JAS2539.1>.
- , S. Watanabe, Y. Kawatani, Y. Tomikawa, K. Miyazaki, and M. Takahashi, 2009: On the origins of mesospheric gravity waves. *Geophys. Res. Lett.*, **36**, L19801, <https://doi.org/10.1029/2009GL039908>.
- , S. Tateno, S. Watanabe, and Y. Kawatani, 2012: Gravity wave characteristics in the Southern Hemisphere revealed by a high-resolution middle-atmosphere general circulation model. *J. Atmos. Sci.*, **69**, 1378–1396, <https://doi.org/10.1175/JAS-D-11-0101.1>.
- Satomura, T., and K. Sato, 1999: Secondary generation of gravity waves associated with the breaking of mountain waves. *J. Atmos. Sci.*, **56**, 3847–3858, [https://doi.org/10.1175/1520-0469\(1999\)056<3847:SGOGWA>2.0.CO;2](https://doi.org/10.1175/1520-0469(1999)056<3847:SGOGWA>2.0.CO;2).
- Schäfler, A., and Coauthors, 2018: The North Atlantic Waveguide and Downstream Impact Experiment. *Bull. Amer. Meteor. Soc.*, **99**, 1607–1637, <https://doi.org/10.1175/BAMS-D-17-0003.1>.
- Shen, X., L. Wang, and S. Osprey, 2020: Tropospheric forcing of the 2019 Antarctic sudden stratospheric warming. *Geophys. Res. Lett.*, **47**, e2020GL089343, <https://doi.org/10.1029/2020GL089343>.
- Siskind, D. E., S. D. Eckermann, J. P. McCormack, L. Coy, K. W. Hoppel, and N. L. Baker, 2010: Case studies of the mesospheric response to recent minor, major, and extended stratospheric warmings. *J. Geophys. Res.*, **115**, D00N03, <https://doi.org/10.1029/2010JD014114>.
- Smith, R. B., and C. G. Kruse, 2017: Broad-spectrum mountain waves. *J. Atmos. Sci.*, **74**, 1381–1402, <https://doi.org/10.1175/JAS-D-16-0297.1>.
- , and —, 2018: A gravity wave drag matrix for complex terrain. *J. Atmos. Sci.*, **75**, 2599–2613, <https://doi.org/10.1175/JAS-D-17-0380.1>.
- , and Coauthors, 2016: Stratospheric gravity wave fluxes and scales during DEEPWAVE. *J. Atmos. Sci.*, **73**, 2851–2869, <https://doi.org/10.1175/JAS-D-15-0324.1>.
- SPARC, 2010: SPARC CCMVal report on the evaluation of chemistry-climate models. SPARC Rep. 5, 426 pp.
- Stevens, B., and Coauthors, 2019: A high-altitude long-range aircraft configured as a cloud observatory: The NARVAL expeditions. *Bull. Amer. Meteor. Soc.*, **100**, 1061–1077, <https://doi.org/10.1175/BAMS-D-18-0198.1>.
- Stober, G., and J. L. Chau, 2015: A multistatic and multifrequency novel approach for specular meteor radars to improve wind measurements in the MLT region. *Radio Sci.*, **50**, 431–442, <https://doi.org/10.1002/2014RS005591>.
- Unger mann, J., and Coauthors, 2011: A 3-D tomographic retrieval approach with advection compensation for the air-borne limb-imager GLORIA. *Atmos. Meas. Tech.*, **4**, 2509–2529, <https://doi.org/10.5194/amt-4-2509-2011>.
- Vaisala, 2020: Vaisala radiosonde RS41-SG. Vaisala Doc., 2 pp., www.vaisala.com/sites/default/files/documents/RS41-SG-Datasheet-B211321EN.pdf.
- Vincent, R. A., and I. M. Reid, 1983: HF Doppler measurements of mesospheric gravity wave momentum fluxes. *J. Atmos. Sci.*, **40**, 1321–1333, [https://doi.org/10.1175/1520-0469\(1983\)040<1321:HDMOMG>2.0.CO;2](https://doi.org/10.1175/1520-0469(1983)040<1321:HDMOMG>2.0.CO;2).
- Voigt, C., and Coauthors, 2017: ML-CIRRUS: The airborne experiment on natural cirrus and contrail cirrus with the high-altitude long-range research aircraft HALO. *Bull. Amer. Meteor. Soc.*, **98**, 271–288, <https://doi.org/10.1175/BAMS-D-15-00213.1>.
- Vosper, S. B., 2015: Mountain waves and wakes generated by south Georgia: Implications for drag parametrization. *Quart. J. Roy. Meteor. Soc.*, **141**, 2813–2827, <https://doi.org/10.1002/qj.2566>.
- Wendisch, M., and Coauthors, 2016: ACRIDICON-CHUVA campaign: Studying tropical deep convective clouds and precipitation over Amazonia using the new German research aircraft HALO. *Bull. Amer. Meteor. Soc.*, **97**, 1885–1908, <https://doi.org/10.1175/BAMS-D-14-00255.1>.
- Wildmann, N., R. Eckert, A. Dörnbrack, S. Gisinger, A. van Niekerk, K. Ohlmann, and M. Rapp, 2021: In situ measurements of wind and turbulence by a motor glider in the Andes. *J. Atmos. Oceanic Technol.*, <https://doi.org/10.1175/JTECH-D-20-0137.1>, in press.
- Wilms, H., M. Bramberger, and A. Dörnbrack, 2020: Observation and simulation of mountain wave turbulence above Iceland: Turbulence intensification due to wave interference. *Quart. J. Roy. Meteor. Soc.*, **146**, 3326–3346, <https://doi.org/10.1002/qj.3848>.
- Woiwode, W., and Coauthors, 2018: Mesoscale fine structure of a tropopause fold over mountains. *Atmos. Chem. Phys.*, **18**, 15643–15667, <https://doi.org/10.5194/acp-18-15643-2018>.
- Wu, D. L., and S. D. Eckermann, 2008: Global gravity wave variances from Aura MLS: Characteristics and interpretation. *J. Atmos. Sci.*, **65**, 3695–3718, <https://doi.org/10.1175/2008JAS2489.1>.